Draft version April 7, 2024
Typeset using LaTeX **twocolumn** style in AASTeX62

arXiv:1811.02568v1 [astro-ph.GA] 6 Nov 2018

BAT AGN Spectroscopic Survey – XI. The Covering Factor of Dust and Gas in *Swift*/BAT Active Galactic Nuclei

Kohei Ichikawa,[1,2,3,4] Claudio Ricci,[5,6,7] Yoshihiro Ueda,[8] Franz E. Bauer,[9,10,11] Taiki Kawamuro,[12,*] Michael J. Koss,[13] Kyuseok Oh,[8,*] David J. Rosario,[14] T. Taro Shimizu,[15] Marko Stalevski,[16,17] Lindsay Fuller,[2] Christopher Packham,[2,12] and Benny Trakhtenbrot[18,19]

[1] *Department of Astronomy, Columbia University, 550 West 120th Street, New York, NY 10027, USA*
[2] *Department of Physics and Astronomy, University of Texas at San Antonio, One UTSA Circle, San Antonio, TX 78249, USA*
[3] *Frontier Research Institute for Interdisciplinary Sciences, Tohoku University, Sendai, Miyagi 980-8578, Japan*
[4] *Astronomical Institute, Tohoku University, Aramaki, Aoba-ku, Sendai, Miyagi 980-8578, Japan*
[5] *Núcleo de Astronomía de la Facultad de Ingeniería, Universidad Diego Portales, Av. Ejército Libertador 441, Santiago, Chile*
[6] *Kavli Institute for Astronomy and Astrophysics, Peking University, Beijing 100871, China*
[7] *Chinese Academy of Sciences South America Center for Astronomy, Camino El Observatorio 1515, Las Condes, Santiago, Chile*
[8] *Department of Astronomy, Kyoto University, Oiwake-cho, Sakyo-ku, Kyoto 606-8502, Japan*
[9] *Institute of Astrophysics, Pontificia Universidad Catolica de Chile, Avenida Vicua Mackenna 4860, 7820436, Chile*
[10] *Millennium Institute of Astrophysics (MAS), Nuncio Monseñor Sótero Sanz 100, Providencia, Santiago, Chile*
[11] *Space Science Institute, 4750 Walnut Street, Suite 205, Boulder, Colorado 80301, USA*
[12] *National Astronomical Observatory of Japan, 2-21-1 Osawa, Mitaka, Tokyo 181-8588, Japan*
[13] *Eureka Scientific, 2452 Delmer Street Suite 100, Oakland, CA 94602-3017, USA*
[14] *Department of Physics, Durham University, South Road, DH1 3LE Durham, UK*
[15] *Max-Planck-Institut für extraterrestrische Physik, Postfach 1312, 85741, Garching, Germany*
[16] *Astronomical Observatory, Volgina 7, 11060 Belgrade, Serbia*
[17] *Sterrenkundig Observatorium, Universiteit Gent, Krijgslaan 281-S9, Gent B-9000, Belgium*
[18] *Department of Physics, ETH Zurich, Wolfgang-Pauli-Strasse 27, CH-8093 Zurich, Switzerland*
[19] *School of Physics and Astronomy, Tel Aviv University, Tel Aviv 69978, Israel*

ABSTRACT

We quantify the luminosity contribution of active galactic nuclei (AGN) to the 12 μm, mid-infrared (MIR; 5-38 μm), and the total IR (5–1000 μm) emission in the local AGN detected in the all-sky 70-month *Swift*/Burst Alert Telescope (BAT) ultra hard X-ray survey. We decompose the IR spectral energy distributions (SEDs) of 587 objects into AGN and starburst components using AGN torus and star-forming galaxy templates. This enables us to recover the AGN torus emission also for low-luminosity end, down to $\log(L_{14-150}/\mathrm{erg\ s^{-1}}) \simeq 41$, which typically have significant host galaxy contamination. We find that the luminosity contribution of the AGN to the 12 μm, the MIR, and the total IR band is an increasing function of the 14–150 keV luminosity. We also find that for the most extreme cases, the IR pure-AGN emission from the torus can extend up to 90 μm. The obtained total IR AGN luminosity through the IR SED decomposition enables us to estimate the fraction of the sky obscured by dust, i.e., the dust covering factor. We demonstrate that the median of the dust covering factor is always smaller than that of the X-ray obscuration fraction above the AGN bolometric luminosity of $\log(L_{\mathrm{bol}}^{(\mathrm{AGN})}/\mathrm{erg\ s^{-1}}) \simeq 42.5$. Considering that X-ray obscuration fraction is equivalent to the covering factor coming from both the dust and gas, it indicates that an additional neutral gas component, along with the dusty torus, is responsible for the absorption of X-ray emission.

Keywords: galaxies: active — galaxies: nuclei — infrared: galaxies

1. INTRODUCTION

One of the fundamental open questions of extra-galactic astrophysics is how supermassive black holes (SMBHs) and their host galaxies co-evolve (e.g., Alexander & Hickox 2012). Active galactic nuclei (AGN) are

Corresponding author: Kohei Ichikawa
k.ichikawa@astr.tohoku.ac.jp

* JSPS fellow

the best targets to understand this process of coevolution, because they are in the stage where the mass accretion onto SMBHs occurs by releasing large amounts of radiation (e.g., Yu & Tremaine 2002; Marconi et al. 2004), until they reach their achievable maximum mass of $M_{\rm BH} \simeq 10^{10.5} M_{\odot}$ (Netzer 2003; McLure & Dunlop 2004; Trakhtenbrot 2014; Jun et al. 2015; Inayoshi & Haiman 2016; Ichikawa & Inayoshi 2017).

Ultra-hard ($E > 10$ keV) X-ray observations are one of the most reliable methods for identifying AGN. Thanks to the combination of (1) a strong penetration power up to $\log(N_{\rm H}/{\rm cm}^{-2}) \simeq 24$ (e.g., Ricci et al. 2015) and (2) the high contrast over stellar X-ray emission (e.g., Mineo et al. 2012), the ultra-hard X-ray surveys allow the potential for an unbiased census of AGN up to Compton-thick levels (e.g., Koss et al. 2016). Among the recent available surveys, *Swift*/BAT provides the most sensitive X-ray survey of the whole sky in the 14–195 keV range, reaching a flux level of (1.0–1.3)$\times 10^{-11}$ erg s^{-1} cm^{-2} in the first 70 months of operations (Baumgartner et al. 2013), and to the deeper flux of (7.2–8.4)$\times 10^{-12}$ erg s^{-1} cm^{-2} in the recently updated 105-month catalog (Oh et al. 2018).

Infrared (IR) observations also provide an effective method to study AGN because the central engine of AGN is expected to be surrounded by a dusty "torus" (Krolik & Begelman 1986) which is heated by the AGN and re-emits thermally in the mid-IR (MIR) (e.g., Gandhi et al. 2009; Asmus et al. 2015; Ichikawa et al. 2012, 2017). A recent upward revision of black hole scaling relations (Kormendy & Ho 2013) indicates that the local mass density in black holes should be higher, suggesting that a larger population of heavily obscured AGN gas and dust is required to fill the mass gap of the revised local black hole mass density (e.g., Novak 2013; Comastri et al. 2015). These populations contribute significantly to the infrared background (e.g., Murphy et al. 2011; Delvecchio et al. 2014), especially in the MIR band (Risaliti et al. 2002). However, since star formation from the host galaxy sometimes contaminates the MIR emission, especially for low-luminosity AGN with $L_{14-150} < 10^{43}$ erg s^{-1} (e.g., Ichikawa et al. 2017), and the torus is too compact (< 10 pc; eg., Jaffe et al. 2004) to be fully resolved (e.g., García-Burillo et al. 2016; Imanishi et al. 2018), the precise estimation of AGN thermal activity is not straightforward.

Fortunately, several methods have been proposed to isolate the torus emission from the starburst component. One of them is to use high spatial resolution ($\sim$0.″3–0.″7) MIR observations to resolve the starburst emission of the host galaxies down to 10 pc scales (Packham et al. 2005; Radomski et al. 2008; Hönig et al. 2010; Ramos Almeida et al. 2011; Alonso-Herrero et al. 2011; González-Martín et al. 2013; Asmus et al. 2014; Ichikawa et al. 2015; Alonso-Herrero et al. 2016; Martínez-Paredes et al. 2017). In addition, the advent of IR interferometry observations, with their exquisite resolving power (with baselines up to 130 m), has spatially resolved the dusty nuclear region and shown that their outer radii in the MIR are typically several pc (e.g., Jaffe et al. 2004; Raban et al. 2009; Burtscher et al. 2013). Notably, some show the polar elongated dust emission suggestive of the dusty outflows (Hönig et al. 2012, 2013; Tristram et al. 2014; López-Gonzaga et al. 2016). However, because of the limited sensitivity and the spatial resolution of current telescopes (see a recent review of Burtscher et al. 2016), these two methods are available only for a few tens of bright sources located in the very local Universe ($z < 0.01$).

Another possible approach is to separate the spectral emission of the AGN and the starburst (SB) component. Multiple decomposition methods have been applied to MIR spectra, mainly using aromatic features as a proxy of star formation (e.g., Tran et al. 2001; Lutz et al. 2004; Sajina et al. 2007; Alonso-Herrero et al. 2012; Ichikawa et al. 2014; Hernán-Caballero et al. 2015; Kirkpatrick et al. 2015; Symeonidis et al. 2016), to broadband IR spectral energy distributions (SEDs, e.g., Hatziminaoglou et al. 2008; da Cunha et al. 2008; Xu et al. 2015; Lyu et al. 2016, 2017; Shimizu et al. 2017), and to the combination of both spectra and SEDs (e.g., Mullaney et al. 2011). The advantage of the SED decomposition is that it is less affected by the differing spatial resolutions inherent in aperture photometry, and can be applied to high-z sources (e.g., Stanley et al. 2015; Mateos et al. 2016; Lyu et al. 2016) and/or to large ($N > 100$) samples, for which high-spatial resolution MIR imaging and spectroscopy would require significant amounts of large diameter (> 8 m) telescope time.

In this paper, we decompose the IR SEDs of ultra-hard X-ray selected *Swift*/BAT 70-month AGN catalog (Baumgartner et al. 2013) into AGN and host galaxy components. Thanks to the intensive follow-up observations by the BAT AGN Spectroscopic Survey[1] (BASS; Koss et al. 2017; Lamperti et al. 2017; Ricci et al. 2017b), we are able to obtain the reliable information on the gas column density ($N_{\rm H}$), absorption corrected 14–150 keV X-ray luminosity (L_{14-150}), and black hole mass ($M_{\rm BH}$) of the sample.

The main goal of this work is to quantitatively assess the AGN contribution to 12 μm, MIR (5–

[1] www.bass-survey.com

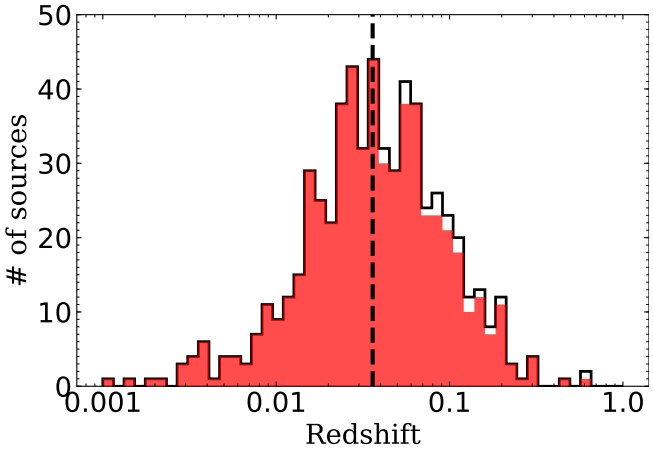

Figure 1. Redshift distribution of AGN in the *Swift*/BAT 70-month catalog at galactic latitude of $|b| > 10°$ (black solid line: 606 objects; see also Ichikawa et al. (2017)) and of those used in this study (red color area: 587 objects). The vertical dashed line represents the median of the redshift ($\langle z \rangle = 0.037$) in our sample.

38 μm) band, and total IR (5–1000 μm) band down to $\log(L_{14-150}/\mathrm{erg\ s^{-1}}) \simeq 41$ in order to investigate 1) the MIR/X-ray luminosity correlation and 2) the dust covering factor of the torus, avoiding issues related to host galaxy contamination. Throughout the paper, we adopt standard cosmological parameters ($H_0 = 70.0$ km s^{-1} Mpc^{-1}, $\Omega_{\rm M} = 0.3$, and $\Omega_\Lambda = 0.7$).

2. SAMPLE

Our initial sample is based on the sample of Ichikawa et al. (2017), which contains the 606 non-blazar AGN from the *Swift*/BAT 70-month catalog (Baumgartner et al. 2013) at galactic latitudes ($|b| > 10°$) for which secure spectroscopic redshifts are available. In this study, we use the column density and the absorption corrected 14–150 keV luminosity tabulated in Ricci et al. (2017b). They are also summarized in Table 1.

In Ichikawa et al. (2017), we reported the 3–500 μm IR counterparts for our AGN sample: utilizing the IR catalogs obtained from *WISE* (Wright et al. 2010; Cutri et al. 2013), *AKARI* (Murakami et al. 2007), *IRAS* (Beichman et al. 1988), and *Herschel* (Poglitsch et al. 2010; Griffin et al. 2010). Out of the 606 sources, we identified 604, 560, 601, and 402 counterparts in the total IR, near-IR (< 5 μm), MIR, and far-IR (FIR; $60-500$ μm) band, respectively. The reader should refer to Ichikawa et al. (2017) for details on the IR catalogs. While Ichikawa et al. (2017) compiled the representative fluxes at 12, 22, 70, and 90 μm, by combining similar wavelength bands in the multiple IR catalogs listed above, in this study we regard each IR band with different central wavelength as independent photometry. Therefore, the available IR photometric bands are at most 17 bands between 3–500 μm, as identified in Table 1. For the data points with the same wavelengths (i.e., 12, 25, 60, 100, and 160 μm), the adopted photometry was chosen based on the priorities reported in the IR catalog of Ichikawa et al. (2017) to measure the IR emission from both nucleus and host galaxy in a uniform way for the entire AGN sample. The 12 μm flux density was obtained with the following priority: *WISE*, *IRAS*/Point Source Catalog (PSC), and *IRAS*/Faint Source Catalog (FSC); for the 25, 60, and 100 μm flux densities, on the other hand, we followed a different order (*IRAS*/PSC and *IRAS*/FSC), while for the 160 μm flux density we used *Herschel*/PACS and, when not available, *AKARI*/FIS.

The corrected data are obtained from a wide range of different angular resolution from *Herschel*/PACS (70 μm; 6 arcsec) to *IRAS*/FIR (100 μm; ≈ 1 arcmin). Using nearly the same sample, Mushotzky et al. (2014) already showed that the bulk of PACS 70 μm is point-like at the spatial resolution of *Herschel*, suggesting that the FIR emission from the host galaxy is really compact (with a median value of 2 kpc FWHM) and unresolvable for most of our sample. Thus, we conclude that the aperture dependence with more moderate resolutions obtained by *AKARI* and *IRAS* is negligible (see also Meléndez et al. 2014 and Ichikawa et al. 2017).

To acquire IR SEDs with a number of data points sufficient for spectral decomposition we require, for each source, at least three photometric bands within the rest-frame 3–500 μm. This is because three data points are needed to define the normalization of the two components (AGN torus and host galaxy). Applying this criteria, our sample is reduced to 588 sources. In addition, we require at least one data point from either the NIR or the FIR band to estimate the host galaxy component, which brings the sample to 587 sources. This is the final sample used for this study, and it represents a large fraction of the initial sample ($587/606 = 97\%$). The redshift distribution of the sample is shown in Figure 1.[2]

We divide the sample into two AGN types based on $N_{\rm H}$ obtained by Ricci et al. (2017b). We define the AGN with $N_{\rm H} < 10^{22}$ cm^{-2} as unobscured AGN, and the AGN with $N_{\rm H} \geq 10^{22}$ cm^{-2} as obscured. Overall we have 300 unobscured and 287 obscured AGN. The AGN type for the complete BAT 70-month catalog are tabulated in Ricci et al. (2017b), as well as in Table 1. We note that Koss et al. (2017) found a 95% agreement for the unobscured and obscured AGN with the presence

[2] M81 is not shown in the figure due to its very low redshift of $z = 10^{-4}$ (see also Ricci et al. 2017b).

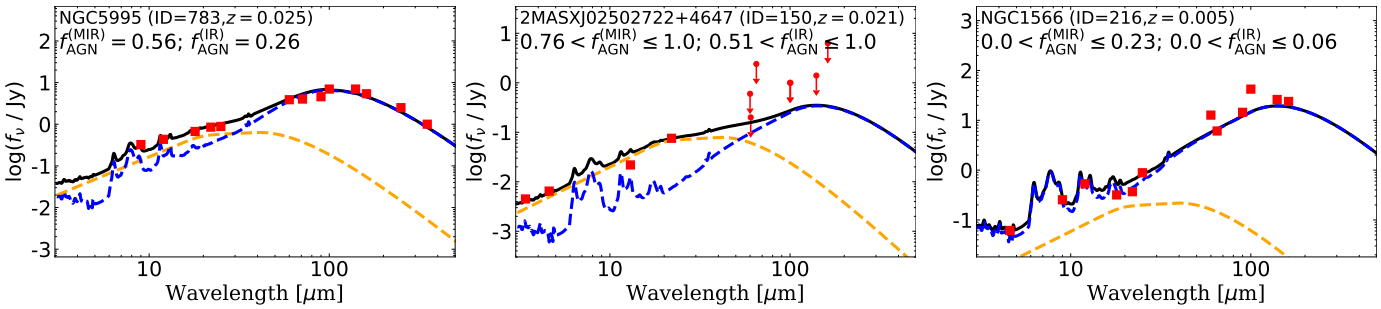

Figure 2. Example of our IR SEDs and their best-fit models. The orange/blue dashed curve represents fitted the AGN/host galaxy template, respectively. The black solid curve is the combination of AGN and host galaxy template, while the red squares with error bars are the flux densities. Each panel also shows the object ID based on the *Swift*/BAT 70-month catalog, the redshift, and the luminosity contribution of the AGN to the MIR ($f_{\rm AGN}^{\rm (MIR)}$) and IR bands ($f_{\rm AGN}^{\rm (IR)}$). All the SEDs of our sample are shown in the Appendix D. Left panel: an example of a source showing both of AGN and host galaxy contributions. Middle panel: an example of an AGN torus-dominated SED. The host galaxy template is plotted as an upper-limit. Right panel: an example of a source with an host galaxy-dominated SED, with the AGN template plotted as an upper-limit.

of a broad Hβ line for optical types Seyfert 1–1.8 and Seyfert 2.

3. ANALYSIS

We decompose the IR SEDs of AGN using SB and AGN templates to estimate the intrinsic AGN IR luminosity. We use the IDL script `DecompIR` coded by Mullaney et al. (2011) and further developed by Del Moro et al. (2013). This code accepts IR photometry points in the 3–500 μm range as input and properly accounts for the filter and instrument response functions of the photometry points. It then computes the approximate levels of AGN and host-galaxy contribution by fitting the data combining a host-galaxy component with an AGN. `DecompIR` contains the mean AGN template produced from the *Swift*/BAT 9-month catalog (Tueller et al. 2008), which broadly traces the typical spectral forms of face-on and edge-on clumpy torus models (e.g., Nenkova et al. 2008a,b) as shown in Mullaney et al. (2011). It also includes the five star-forming galaxy templates (Mullaney et al. 2011; Del Moro et al. 2013), using the average starburst SEDs derived by Dale et al. (2001). The five galaxy templates are composites of local star-forming galaxies with $L_{\rm IR} < 10^{12}\ L_\odot$ (Brandl et al. 2006). They characterize well the full range of host-galaxy SED shapes (Del Moro et al. 2013; Stanley et al. 2015), such as the galaxy template library of Chary & Elbaz (2001). Using these representative templates, we are able to fit the data without suffering from the degeneracy of the fitting procedure caused by the large number of templates. In addition, as some of our sources have only three data points, it is reasonable to keep the number of free parameters as small as possible.

The free parameters of the fitting are the normalizations of the AGN and of the host-galaxy templates; therefore at least three IR data points are needed to fit the SEDs. However, only for the very luminous sources, we added one more free parameter. It is known that, in high-luminosity AGN, the IR SEDs become much flatter at shorter wavelengths, which could be related to the stronger radiation field heating the surrounding dust to higher temperatures compared to moderate-luminosity AGN (e.g., Richards et al. 2006; Netzer et al. 2007; Mullaney et al. 2011; Symeonidis et al. 2016; Lyu et al. 2017; Lani et al. 2017). Our AGN SEDs also show such tendency, especially at high luminosities ($L_{14-150} > 10^{44}$ erg s^{-1}). Therefore, for the sources which have at least four data points and luminosities $L_{14-150} > 10^{44}$ erg s^{-1}, we also allow the spectral index α_1 of the AGN template (see Mullaney et al. 2011) to be shallower at wavelength shorter than 19 μm.

To determine the best fitting parameters, we first fit the SED by using the five host galaxy templates (SB1–SB5) and the AGN template. We then check the results obtained using the five different SB templates, and we choose the one providing the best results according to the chi-squared statistic (χ^2) minimization.

Figure 2 shows examples of the best-fitting SEDs that include both the AGN and star formation components, together with the best-fitting SEDs requiring only the host galaxy or the AGN component. All the other SEDs of our sample are compiled in the Appendix D. Overall, 474 sources required both the AGN and the host galaxy templates, while 94 sources required only the AGN template. For the latter objects, the fitting quality does not improve even when including an additional SB template. Since most of those sources (89 out of the 94 sources) are not detected in the FIR bands, and considering that the FIR bands have shallower sensitivities than the MIR ones, the lack of a significant contribution

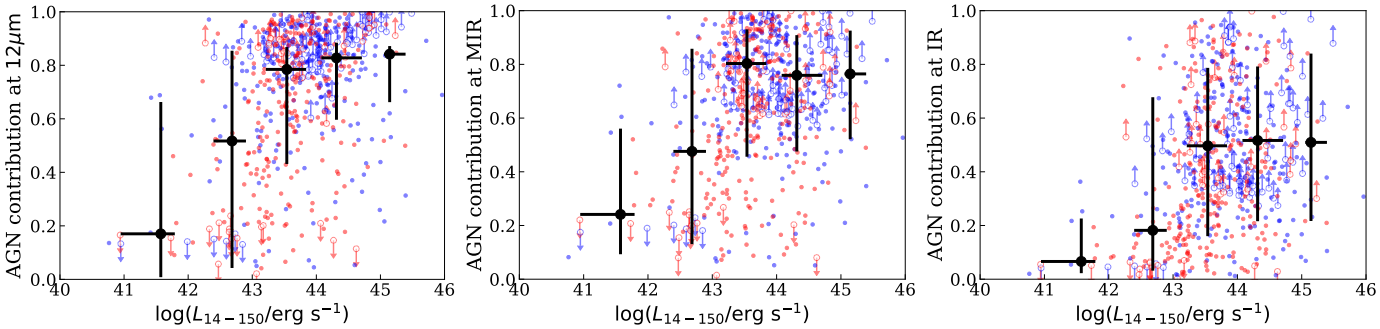

Figure 3. Fractional luminosity contribution of AGN to the 12 μm (left), MIR (middle), and total IR (right) luminosity, as a function of 14–150 keV luminosity (L_{14-150}). The blue (unobscured AGN) and red (obscured AGN) circles represent individual sources. The circles with lower/upper-limits represent the sources that require only the AGN or host galaxy template, as discussed in Section 3. The black crosses represent the median contribution of the AGN luminosity in each bin of L_{14-150}, with the error bars showing the inter-percentage range with 68.2% of the sample.

of the SB template in the MIR does not always imply that the host galaxy does not contribute to the total IR luminosity. In order to assess how much the host galaxy could contribute to the total infrared luminosity without affecting the observed SEDs, we calculate the upper limits on the star formation contribution by following Stanley et al. (2015), where the same SED decomposition routine, `DecompIR`, was used. This was done by increasing the normalization of the host galaxy template until it reached one of the upper limits, or exceeded the 3σ uncertainty of a data point. We then used the star-forming galaxy template giving the highest value of IR luminosity as our conservative upper limit. For the sources which have an upper limit on the host galaxy component, we show the lower limit values of the AGN contribution to the MIR flux (5–38 μm; $f_{\rm AGN}^{\rm (MIR)}$) and to the total IR flux (5–1000 μm; $f_{\rm AGN}^{\rm (IR)}$) in each SED, as illustrated in the middle panel of Figure 2. The lower-limits on $f_{\rm AGN}^{\rm (MIR)}$ and $f_{\rm AGN}^{\rm (IR)}$ are reported in Table 1, and readers can use the flag (`flag_limit`) to assess whether the values are lower-limits or not.

There are 18 sources in our sample which were best-fit to the host galaxy template alone ($f_{\rm AGN}^{\rm (MIR)}=0$). Again, in order to assess the contribution of AGN to the total IR luminosity, we calculate the upper limits on the AGN torus contribution with the same methods of the AGN dominated SEDs, as discussed above. The upper limits of $f_{\rm AGN}^{\rm (MIR)}$ and $f_{\rm AGN}^{\rm (IR)}$ are also shown in the right panel of Figure 2 (see also Table 1).

Using this SED fitting approach, we have measurements of the AGN luminosity in the 12 μm ($L_{12\ \mu{\rm m}}^{\rm (AGN)}$), MIR ($L_{\rm MIR}^{\rm (AGN)}$) and total IR bands ($L_{\rm IR}^{\rm (AGN)}$). All the values, as well as the IR flux densities, are tabulated in Table 1. We do not compile the IR star forming luminosity, due to the impossibility of obtaining a reliable estimates for the sources not detected in the FIR.

4. RESULTS AND DISCUSSION

4.1. *Fractional Luminosity Contribution of AGN to the IR Band*

Figure 3 shows the median of the AGN contribution to the 12 μm, MIR, and total IR luminosities as a function of L_{14-150}. The AGN contribution is calculated from the ratio between the AGN and the total (SF plus AGN) luminosity:

$$f_{\rm AGN}^{\rm (12\mu m,MIR,IR)} = L_{\rm 12\mu m,MIR,IR}^{\rm (AGN)}/(L_{\rm 12\mu m,MIR,IR}^{\rm (AGN)}+L_{\rm 12\mu m,MIR,IR}^{\rm (SF)}). \quad (1)$$

Figure 3 shows that the luminosity contribution of the AGN to the 12 μm, MIR, and to the total IR band increases with L_{14-195}. On the low-luminosity end ($L_{14-195}<10^{43}$ erg s^{-1}), Figure 3 indicates that the host galaxy emission significantly contaminates ($\simeq$ 50–80%) the 12 μm and MIR band. On the high luminosity end ($L_{14-195}>10^{43}$ erg s^{-1}), it clearly shows that the AGN component is the dominant ($\gtrsim$ 80%) energy source at 12 μm and in the MIR band. This overall result is broadly consistent with the previous studies which explored the AGN contribution using high spatial resolution imaging (e.g., Asmus et al. 2011, 2014, and references therein). These works are discussed in the Appendix A.1. On the other hand, in the total IR band, the AGN component contributes only up to $\simeq$ 50% even at high luminosities. This result is consistent with the calculations of local quasars (Lyu et al. 2017), where it is shown that AGN contribute to $\simeq$ 50% of the flux even if they provide 90% of the MIR emission.

Figure 3 also shows that the scatter of the percentage for $f_{\rm AGN}^{\rm (MIR)}$ is $\sim$ 20% and increases up to $\sim$ 35% for $f_{\rm AGN}^{\rm (IR)}$. The origin of the scatter is mostly due to AGN-dominated sources without any detections in the FIR bands. Since the distant sources with $z>0.05$ have not been observed with *Herschel* (see Meléndez et al.

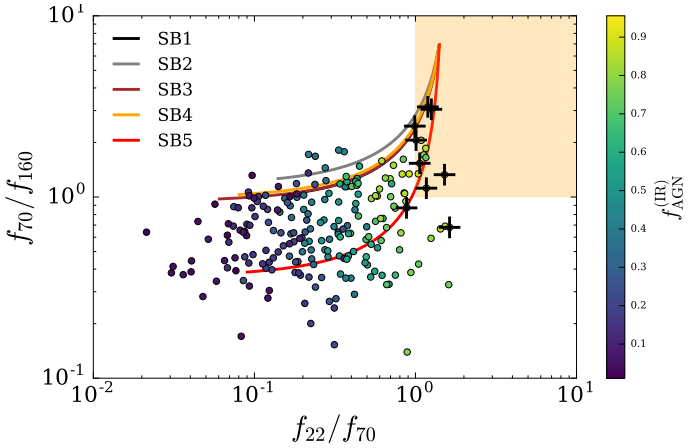

Figure 4. Observed $f_{70\ \mu m}/f_{160\ \mu m}$ versus $f_{22\ \mu m}/f_{70\ \mu m}$ ratio for sample sources with secure detections in the 22 μm, 70 μm, and 160 μm bands. The color-color variations as a function of $f_{\rm AGN}^{\rm (IR)}$ are also plotted for the five SB templates used in this study originated from Mullaney et al. (2011). The black crosses are the IR pure-AGN sources discussed in Section 4.2. The colorbar represents the AGN contribution to the total IR band ($f_{\rm AGN}^{\rm (IR)}$). The orange area illustrates the region with $f_{22\ \mu m} > f_{70\ \mu m} > f_{160\ \mu m}$.

2014; Shimizu et al. 2016), those sources have very shallow upper limits: 0.2 Jy at 60 μm (*IRAS*/FSC) and/or 0.55 Jy at 90 μm (*AKARI*/FIS). This allows a possible contribution of the host galaxy emission to the FIR bands, even when its contribution to the MIR flux is negligible as discussed in Section 3 (see also Lyu et al. 2017). Therefore, higher sensitivity FIR photometry is crucial to quantify the host galaxy contribution for those sources.

4.2. *IR Pure-AGN Candidates*

Some sources show AGN-dominated SEDs even in the FIR bands. These sources are called IR pure-AGN (Mullaney et al. 2011; Rosario et al. 2012; Matsuoka & Woo 2015; Ichikawa et al. 2017; Rosario et al. 2018), and are ideal candidates to derive intrinsic AGN IR templates. These IR pure-AGN have a spectral turn-over at 20–40 μm (Alonso-Herrero et al. 2012; Hönig et al. 2014; Fuller et al. 2016; Lopez-Rodriguez et al. 2018), and a declining flux density from 40 μm to 160 μm, suggesting a very low contribution from the starburst in the host galaxy. In order to check the SED turn-over quantitatively, we plot IR color-color plots of $f_{70\ \mu m}/f_{160\ \mu m}$ versus $f_{22\ \mu m}/f_{70\ \mu m}$ in Figure 4. Both flux ratios are known to be sensitive to the SED peak, and therefore to the dust temperature (Meléndez et al. 2014; García-González et al. 2016). The orange shaded area in Figure 4 ($f_{70\ \mu m}/f_{160\ \mu m} > 1.0$ and $f_{22\ \mu m}/f_{70\ \mu m} > 1.0$) indicates a decline in flux density as a function of wavelength from 22 μm to 160 μm since the sources fulfill $f_{22\ \mu m} > f_{70\ \mu m} > f_{160\ \mu m}$.

Figure 4 also shows the simulated IR color as a function of $f_{\rm AGN}^{\rm (IR)}$ for the each SB template. All IR colors follow a similar trend; $f_{22\ \mu m}/f_{70\ \mu m}$ increases up to $f_{22\ \mu m}/f_{70\ \mu m} \simeq 1.0$ with $f_{\rm AGN}^{\rm (IR)}$ up to 0.9, while $f_{70\ \mu m}/f_{160\ \mu m}$ shows a very shallow increase until $f_{\rm AGN}^{\rm (IR)} \leq 0.8$. However, for $f_{\rm AGN}^{\rm (IR)} > 0.9$, $f_{70\ \mu m}/f_{160\ \mu m}$ starts to drastically increase, reaching values up to $\simeq 7.0$. Thus, sources located in the orange shaded area should have AGN-dominated IR SEDs with $f_{\rm AGN}^{\rm (IR)} > 0.90$. In this study we define IR pure-AGN when the source fulfills the following criteria: 1) $f_{\rm AGN}^{\rm (IR)} > 0.90$ and 2) a significant detection both at 60–70 μm and 160 μm. A total of nine sources are selected with these criteria, and are shown with the black crosses in Figure 4. Most IR pure-AGN are successfully located in the orange shaded area in the color-color-plot. Figure 5 shows the SEDs of the selected 9 IR pure-AGN. All sources show an SED turn-over between $\simeq$ 20 μm and $\simeq$ 70 μm, a declining flux density from 70 μm to 160 μm, and do not show any FIR bump due to star formation up to 90 μm, with the exception of Fairall 9 and II SZ 010. Some of the sources of our sample have already been reported as being dominated by torus emission in the IR from the study of their *Spitzer*/IRS spectra (e.g., MCG -05-23-16; Ichikawa et al. 2015), based on the spectral turn-over at 20–40 μm (Alonso-Herrero et al. 2012; Hönig et al. 2014; Fuller et al. 2016; Lopez-Rodriguez et al. 2018).

We also check the AGN properties of IR pure-AGN compared to the parent sample. The means and standard deviations of the logarithmic X-ray luminosity, black hole mass, and Eddington ratio of this subsample are $\langle \log L_{14-150} \rangle = 43.7 \pm 0.3$ $\langle \log M_{\rm BH} \rangle = 7.8 \pm 0.5$, and $\langle \log \lambda_{\rm Edd} \rangle = -1.2 \pm 0.3$, respectively. These values are consistent with those of the parent sample of $\langle \log L_{14-150} \rangle = 43.7 \pm 0.8$, $\langle \log M_{\rm BH} \rangle = 8.0 \pm 0.8$, and $\langle \log \lambda_{\rm Edd} \rangle = -1.5 \pm 0.8$. This result suggests that the dominating AGN contribution to the total IR band is not related to their higher AGN luminosities, lower BH masses, or higher Eddington ratio, while it implies that they have weaker star-formation luminosities than other AGN with similar luminosities. Actually, MCG -05-23-16 is one of the pure IR-AGN whose CO emission has not been detected (Rosario et al. 2018) in the *Swift*/BAT AGN subset of the LLAMA survey (Davies et al. 2015). This suggests that its host galaxy already lacks the molecular gas to produce the star formation. The on-going molecular gas observations conducted by the BASS survey (M. Koss et al. in prep.) will explore

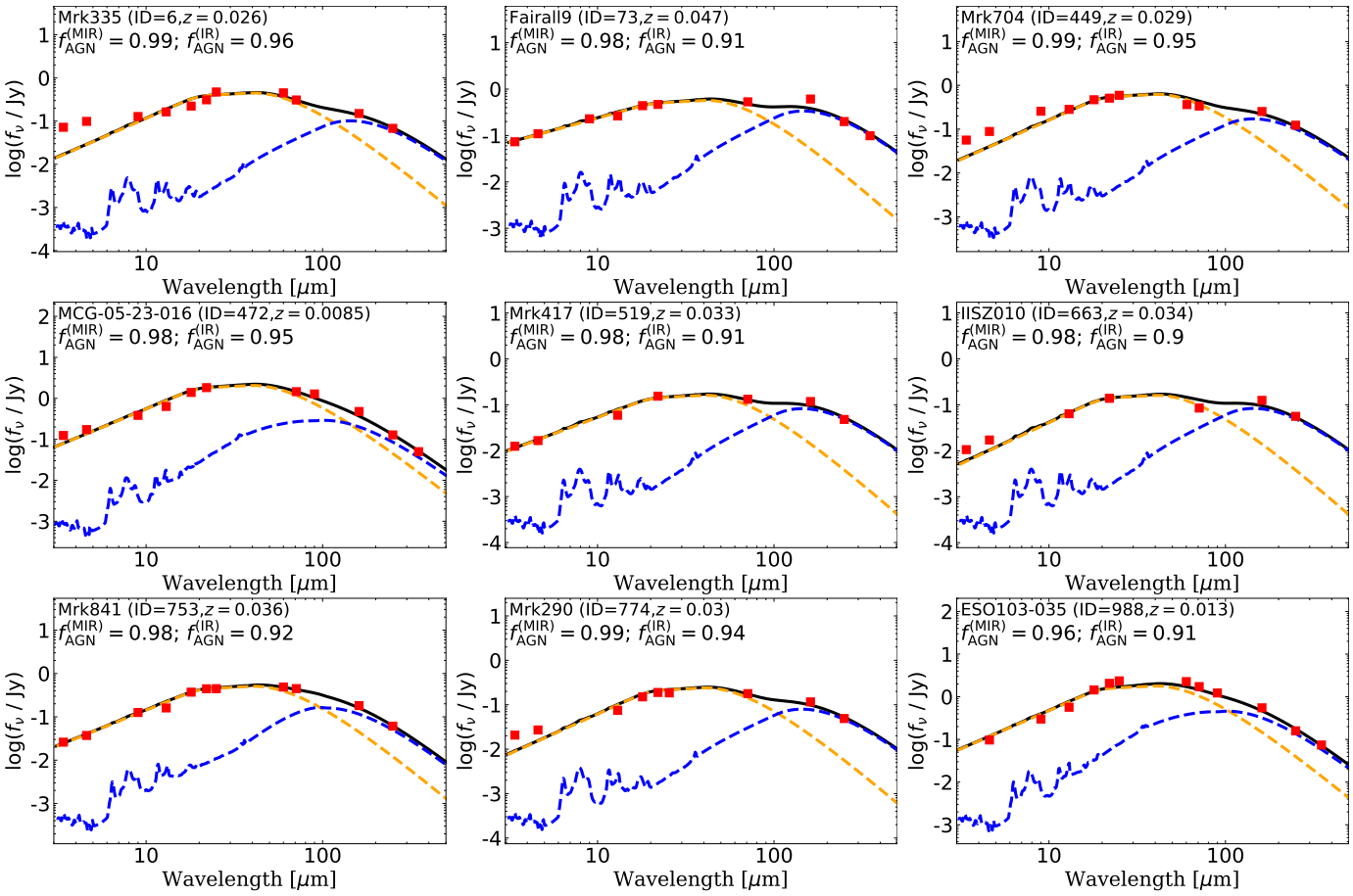

Figure 5. SEDs of the IR pure-AGN candidates defined as 1) $f_{\rm AGN}^{\rm (IR)} > 0.90$ and 2) significant detection both at 60–70 μm and 160 μm. All plots are same as in Figure 2.

the origin of the deficit of star formation in these IR pure-AGN sources.

4.3. *Correlation Between the 12 μm AGN and 14–150 keV Luminosities*

Figure 6 shows the relation between $L_{12\mu\rm m}^{\rm (AGN)}$, $L_{\rm MIR}^{\rm (AGN)}$, and L_{14-150} in the $10^{40} < L_{14-150} < 10^{47}$ erg s^{-1} range. Blue and red crosses represent unobscured and obscured AGN, respectively. The upper limits, shown as open circles, represent the host galaxy dominated sources which have a possible AGN contribution in the 12 μm and MIR band as discussed in Section 3.

The slope of the relation between $L_{12\mu\rm m}^{\rm (AGN)}$, $L_{\rm MIR}^{\rm (AGN)}$ and L_{14-150} is estimated considering the two variables as independent parameters. Since our data contains both detections and upper limits, we apply the survival analysis method using the Python package[3] of ASURV (Feigelson & Nelson 1985; Isobe et al. 1986; Lavalley et al. 1992) to account for the upper limits on $L_{12\mu\rm m}^{\rm (AGN)}$ and $L_{\rm MIR}^{\rm (AGN)}$.

[3] http://python-asurv.sourceforge.net/

We use the slope Bisector fits, which minimize perpendicular distance from the slope line to data points. The fits, with the form of $[\log(L_{12\mu\rm m,MIR}^{\rm (AGN)}/10^{43}\ {\rm erg\ s^{-1}}) = (a \pm \Delta a) + (b \pm \Delta b)\log(L_{14-150}/10^{43}\ {\rm erg\ s^{-1}})]$, where Δa and Δb are the standard deviations of a and b, respectively, result in

$$\log \frac{L_{12\mu\rm m}^{\rm (AGN)}}{10^{43}\ {\rm erg\ s^{-1}}} = (-0.24 \pm 0.03) + (1.08 \pm 0.03) \times \log \frac{L_{14-150}}{10^{43}\ {\rm erg\ s^{-1}}}, \quad (2)$$

$$\log \frac{L_{\rm MIR}^{\rm (AGN)}}{10^{43}\ {\rm erg\ s^{-1}}} = (-0.05 \pm 0.03) + (1.06 \pm 0.03) \times \log \frac{L_{14-150}}{10^{43}\ {\rm erg\ s^{-1}}}, \quad (3)$$

and they are also summarized in Table 2. We find that both luminosity-luminosity and flux-flux correlations are significant (see also Appendix B for the flux-flux correlations).

In Figure 6, some of the fits reported by recent works are also overplotted. Since most previous studies used

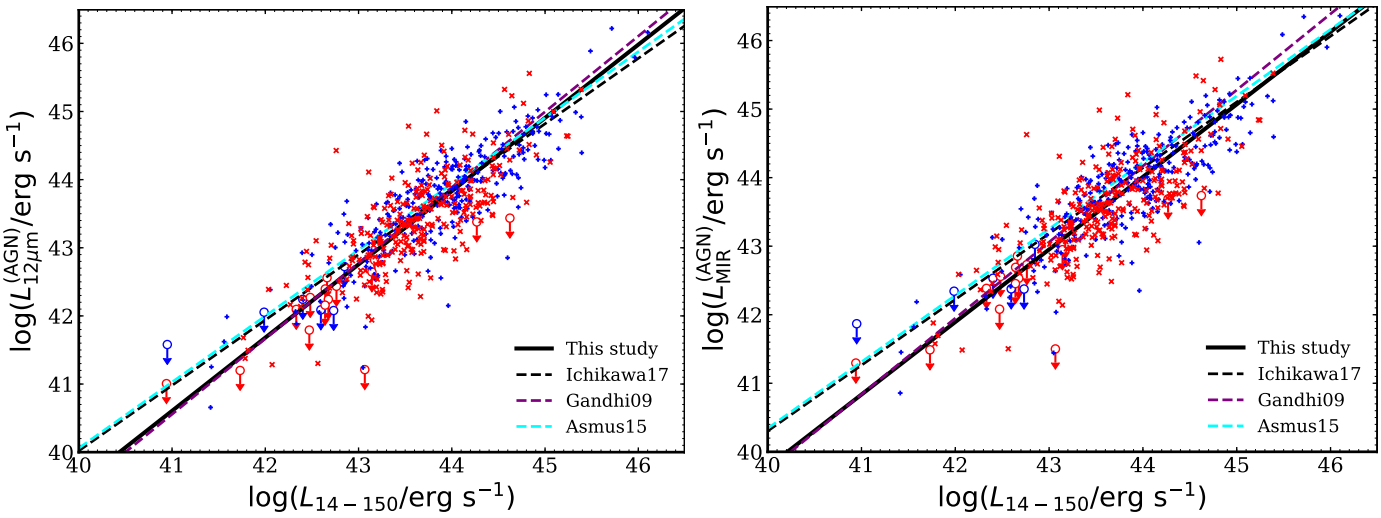

Figure 6. Scatter plot of the 14–150 keV (L_{14-150}) luminosity and the AGN 12 μm ($L_{12\ \mu m}^{(AGN)}$; left panel) and MIR ($L_{MIR}^{(AGN)}$; right panel) luminosities . Blue and red cross represents unobscured and obscured AGN, respectively. The black solid line represents the slope obtained by this study using the infrared bands after the SED decomposition. The other slope represents the one obtained by our previous study; before the SED decomposition (Ichikawa et al. 2017, ; black dashed line), and the higher spatial resolution studies of Gandhi et al. (2009) (purple), and Asmus et al. (2015) (cyan).

the 2–10 keV luminosity, we apply a conversion factor of $L_{14-150}/L_{2-10} = 2.36$ under the assumption of the photon index $\Gamma = 1.8$, which is the median value of the *Swift*/BAT 70-month AGN sample (Ricci et al. 2017b), for overplotting in the same Figure. Since the AGN template used in this study has a ratio of $L_{MIR}^{(AGN)}/L_{12\ \mu m}^{(AGN)} = 1.92$, we also apply it to the slopes from the previous studies for overplotting in the relation between $L_{MIR}^{(AGN)}$ and L_{14-150}.

Compared to Ichikawa et al. (2017), where we found $b = 0.96 \pm 0.02$, the sample used here shows a smaller 12 μm contribution from AGN in the low-luminosity end. This is because the sources with lower L_{14-195} have a significant host galaxy contamination even in the MIR, as shown in Figure 3 and also in the right panel of Figure 11. Indeed, Ichikawa et al. (2017) also reported that the slope becomes slightly steeper with $b = 1.05 \pm 0.03$ when one considers sources with $L_{14-195} > 10^{43}$ erg s^{-1}, for which the host galaxy contamination in the MIR is negligible. This is also consistent with the value of $b = 1.08 \pm 0.03$ in this study.

We compare our results with what was found by Gandhi et al. (2009) and Asmus et al. (2015) using high spatial resolution observations of X-ray selected AGN down to the low-luminosity end. The MIR emission in those studies is most likely dominated from the AGN torus and have a relatively low level of the host galaxy contamination thanks to their spatially resolved images. As shown in Figure 6, our study finds a similar slope to that reported in Gandhi et al. (2009) ($b = 1.11 \pm 0.07$), and also within 3σ uncertainty to that of Asmus et al. (2015) ($b = 0.97 \pm 0.03$). This strongly supports that our SED decomposition method nicely reproduces the high spatial resolution flux, which is thought to be dominated from AGN torus emission.

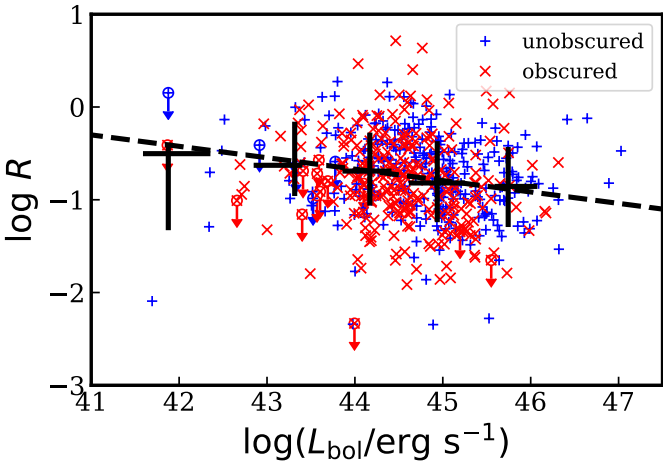

Figure 7. $R = L_{IR}^{(AGN;1-1000\mu m)}/L_{bol}^{(AGN)}$ as a function of the bolometric luminosity. The black crosses represent the median value of R in each bin of the bolometric luminosity, with the error bars showing the inter-percentage range with 68.2% of the sample.

4.4. *Covering Factor of AGN as a Function of Bolometric Luminosity*

The ratio of the AGN IR luminosity and the AGN bolometric luminosity ($R = L_{IR}^{(AGN)}/L_{bol}^{(AGN)}$) has been interpreted as an indirect indicator of the dust cover-

ing factor $C_{\rm T}$(dust), since, for a given AGN luminosity, $L_{\rm IR}^{\rm (AGN)}$ should be proportional to $C_{\rm T}$(dust) ($L_{\rm IR}^{\rm (AGN)} \propto C_{\rm T}({\rm dust}) \times L_{\rm bol}^{\rm (AGN)}$; Maiolino et al. 2007; Treister et al. 2008; Elitzur 2012) . Since the flux of the accretion disk cannot be directly measured for all the sources of our sample, we used L_{14-150} to estimate the bolometric luminosity. We apply a constant bolometric correction of $L_{\rm bol}^{\rm (AGN)}/L_{2-10} = 20$, which is equivalent to $L_{\rm bol}^{\rm (AGN)}/L_{14-150} = 8.47$ under the assumption of $\Gamma = 1.8$, which is the median value of the *Swift*/BAT 70-month AGN sample (Ricci et al. 2017b). We note that our main results do not change significantly when adopting different bolometric corrections, including luminosity-dependent ones (Marconi et al. 2004). We briefly discuss this in Appendix C.2.

To calculate R, we follow in the same manner as Stalevski et al. (2016). We use the total IR AGN luminosity integrated over 1–1000 μm ($L_{\rm IR}^{\rm (AGN;1-1000\mu m)}$) instead of $L_{\rm IR}^{\rm (AGN)}$ integrating the SED over 5–1000 μm. This is because Stalevski et al. (2016) recommend to use the AGN SEDs including near-IR, which sometimes contributes to the total IR luminosity with non-negligible level. Since we do not have IR AGN template down to 1 μm, we extrapolate the AGN template using the same spectral index of α_1 used at wavelength shorter than 19 μm. Therefore, R is calculated based on $R = L_{\rm IR}^{\rm (AGN;1-1000\mu m)}/L_{\rm bol}^{\rm (AGN)}$ in the following study.

Figure 7 shows the relation between R and the AGN bolometric luminosity. The black dashed line represents the fit obtained using ASURV to account for the sources with upper limit:

$$\log R = (4.52 \pm 1.25) + (-0.12 \pm 0.03) \log \left(\frac{L_{\rm bol}^{\rm (AGN)}}{\rm erg\ s^{-1}} \right). \quad (4)$$

This shows that R is a very weak function of AGN bolometric luminosity. However, R does not always represent the actual $C_{\rm T}$(dust), because the standard geometrically-thin and optically-thick disk emits radiation anisotropically (Netzer 1987; Lusso et al. 2013). Thus we also estimate $C_{\rm T}$(dust) exploiting the recent results of Stalevski et al. (2016), who computed the correction function between the covering factor ($C_{\rm T}$(dust)) and R using a clumpy two-phase medium with the sharp boundary between the dusty and dust-free environments. They compute the $C_{\rm T}$(dust)–R relation for a range of equatorial torus thickness ($\tau_{9.7} = 3 - 10$). We consider here the function for $\tau_{9.7} = 3$:

$$C_{\rm T}({\rm dust}) = \begin{cases} -0.178R^4 + 0.875R^3 - 1.487R^2 \\ \qquad +1.408R + 0.192 \ ({\rm type1}) \\ 2.039R^3 - 3.976R^2 + 2.765R + 0.205 \ ({\rm type2}). \end{cases} \quad (5)$$

We use the Equation 5 for type-1/type-2 AGN to un/obscured AGN in this study. According to Stalevski et al. (2016) the relations reported above are valid only for $R \leq R_{\rm max}$, where $R_{\rm max} = 1.3$ for unobscured AGN and $R_{\rm max} = 1.0$ for obscured AGN, so that we removed five sources with $R \geq R_{\rm max}$ from the sample. Figure 8 shows $C_{\rm T}$(dust) as a function of $L_{\rm bol}$.

Besides the dust covering factor $C_{\rm T}$(dust), we also calculate the fraction of obscured AGN ($\log N_{\rm H}/{\rm cm^{-2}} \geq 22.0$), including the Compton-thick sources for each $L_{\rm bol}^{\rm (AGN)}$ bin as shown in Figure 8 (orange crosses). Since X-rays are absorbed by both gas and dust, the fraction of obscured AGN is a proxy of the covering factor of the obscuring material, and is sensitive to both gas and dust [$C_{\rm T}$(gas + dust)] [4]. We follow the same approach to obtain $C_{\rm T}$(gas + dust) of Ricci et al. (2017a). The column density $N_{\rm H}$ for our sample is obtained through the detailed X-ray spectral fitting using the follow-up X-ray observations (Ricci et al. 2017b). In the X-ray fitting, both photoelectric absorption and Compton scattering are considered, and are listed in Table 5 of Ricci et al. (2017b). $C_{\rm T}$(gas + dust) is defined as $C_{\rm T}({\rm gas + dust}) = f_{\rm Cthin} + f_{\rm CT}$, where $f_{\rm Cthin}$ is the fraction of Compton-thin obscured AGN ($22 \leq \log N_{\rm H}/{\rm cm^{-2}} < 24.0$) at each $L_{\rm bol}^{\rm (AGN)}$ bin, while the Compton-thick fraction is $f_{\rm CT} = 0.32$ for $\log(L_{\rm bol}^{\rm (AGN)}/{\rm erg\ s^{-1}}) < 43.5$ and $f_{\rm CT} = 0.21$ for $\log(L_{\rm bol}^{\rm (AGN)}/{\rm erg\ s^{-1}}) > 43.5$ obtained from the intrinsic $N_{\rm H}$ distribution (Ricci et al. 2015). The reason using the $f_{\rm CT}$ above is because even *Swift*/BAT sources are unbiased for $N_{\rm H} < 10^{24}$ cm^{-2}, they can still be affected by obscuration for $N_{\rm H} > 10^{24}$ cm^{-2}.

4.4.1. $L_{\rm bol}^{\rm (AGN)}$-dependent trend of $C_{\rm T}$(dust)

Figure 8 shows that both $C_{\rm T}$(dust) and $C_{\rm T}$(gas + dust) seem to decrease as a function of AGN bolometric luminosity, and, in the high luminosity end, $C_{\rm T}$(gas + dust)

[4] Although the dusty region also contains the gas, in this study we use $C_{\rm T}$(dust) as the dusty covering factor which emits the IR emission heated by AGN. We then use $C_{\rm T}$(gas + dust) as the covering area of gas which is responsible for the X-ray absorption. This region includes 1) the dusty region defined by $C_{\rm T}$(dust) since the dusty region also includes the gas, and 2) the dust-free region inside the sublimation radius, but containing the neutral gas.

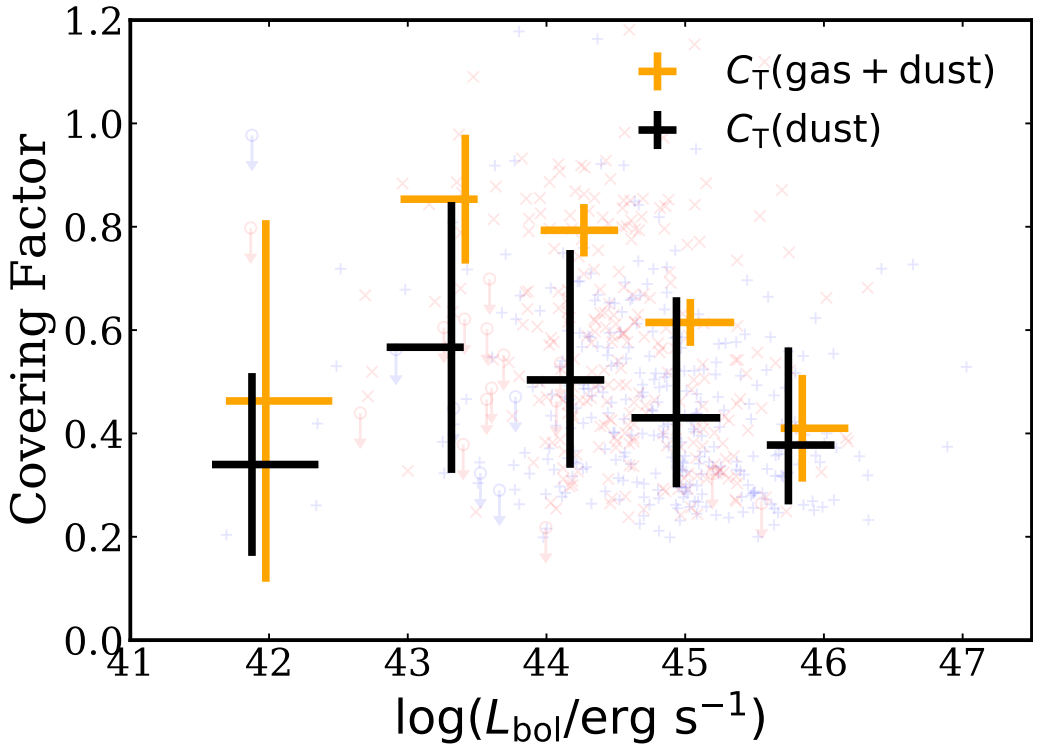

Figure 8. The covering factor (C_T) as a function of the bolometric luminosity. The dust covering factors C_T(dust) are obtained from R using the corrections reported in Stalevski et al. (2016). The covering factor of gas and dust C_T(gas + dust) are obtained from the X-ray observations and the spectral fitting based on the obscured AGN fraction including the Compton-thick AGN (Ricci et al. 2015, 2017b). The Compton-thick fraction is $f_{CT} = 0.32$ for $\log(L_{bol}^{(AGN)}/\mathrm{erg\ s^{-1}}) < 43.5$ and $f_{CT} = 0.21$ for $\log(L_{bol}^{(AGN)}/\mathrm{erg\ s^{-1}}) > 43.5$. The orange crosses are shifted to the right by 0.1 dex for clarity.

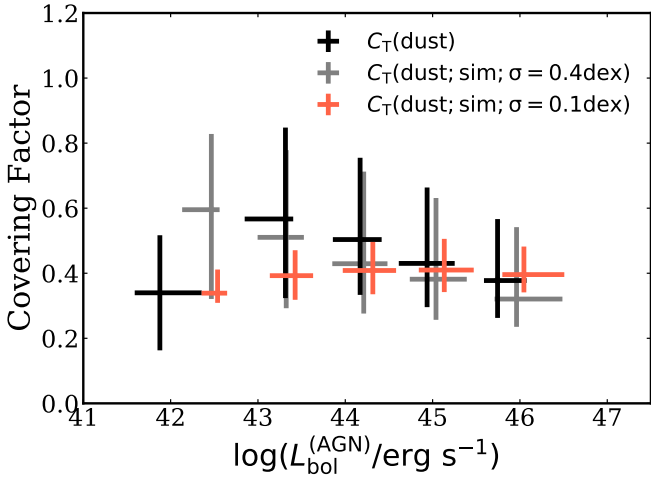

Figure 9. The dust covering factor (C_T(dust)) as a function of the bolometric luminosity. The simulated dust covering factor C_T(dust; sim) are obtained from the simulation using the random population following the $L_{IR}^{(AGN)}$–L_{14-150} relation with scatter of $\sigma = 0.4$ dex (gray crosses) and $\sigma = 0.1$ dex (pink crosses). The gray/pink crosses are shifted to the right by 0.1/0.2 dex for clarity.

finally converge into that of C_T(dust). This luminosity-dependent trend of C_T has been observationally reported in multiple wavelengths from IR (e.g., Maiolino et al. 2007; Alonso-Herrero et al. 2011), to the optical (Simpson 2005), and X-ray (Ueda et al. 2003, 2011, 2014; Beckmann et al. 2009; Ricci et al. 2013).

However, recent studies have found that the luminosity-dependence of C_T(dust) is actually really weak, and that the trend might even disppear after considering some possible biases. Netzer et al. (2016) argues that the reported C_T(dust) would disappear by using different bolometric corrections. Stalevski et al. (2016) also found that the luminosity-dependent trend always mitigates after considering the anisotropy of the torus emission. A similar weak or non-significant luminosity-dependent trend is reported in Mateos et al. (2016), and a more detailed review is given by Netzer (2015).

In order to understand this trend in more detail, we conduct simulations to assess the luminosity dependence of C_T(dust). We first generate two random populations of L_{14-150} for unobscured and obscured AGN for a sample of 10^4 sources with the same number ratio as our parent sample (unobscured/obscured=300/287; see Section 2). Each sample is generated based on our

parent sample, using Gaussian distribution with the median $\log(L_{14-150}/\mathrm{erg\ s^{-1}})$ of $(43.9, 43.6)$ and the standard deviation of of $(0.85\ \mathrm{dex}, 0.67\ \mathrm{dex})$ for unobscured and obscured AGN, respectively. Then the distribution of $L_{\mathrm{IR}}^{(\mathrm{AGN};1-1000\mu\mathrm{m})}$ is calculated under the assumption that two populations follow the luminosity correlation of $L_{\mathrm{IR}}^{(\mathrm{AGN};1-1000\mu\mathrm{m})}$–$L_{14-150}$ with a scatter of $\sigma = 0.4$ dex, and finally the distribution of $C_{\mathrm{T}}(\mathrm{dust})$ is computed in the same manner. The result is shown in Figure 9 that the computed $C_{\mathrm{T}}(\mathrm{dust})$ distribution (gray cross bins) roughly reproduces the luminosity-dependent trend of the black solid bins. Next, we assume that all AGN should follow the luminosity correlation of $L_{\mathrm{IR}}^{(\mathrm{AGN};1-1000\mu\mathrm{m})}$–$L_{14-150}$ and the intrinsic population should have the narrower scatter; down to $\sigma = 0.1$ dex. The results are shown in pink in Figure 9, showing that the luminosity-dependent trend disappears and the binned $C_{\mathrm{T}}(\mathrm{dust})$ is almost constant [$C_{\mathrm{T}}(\mathrm{dust}) \simeq 0.4$] over the entire $L_{\mathrm{bol}}^{(\mathrm{AGN})}$ range. Therefore, we conclude that this seemingly luminosity-dependent trend can be produced purely by the scatter of the distribution, and our results confirm the recent arguments that the luminosity-dependence of $C_{\mathrm{T}}(\mathrm{dust})$ is actually really weak or absent.

4.4.2. *Relation between* $C_{\mathrm{T}}(\mathrm{dust})$ *and* $C_{\mathrm{T}}(\mathrm{gas+dust})$

The other interesting result from the figure is that the $C_{\mathrm{T}}(\mathrm{gas+dust})$ is always same or larger than the binned $C_{\mathrm{T}}(\mathrm{dust})$ over the entire AGN luminosity range. This relation still holds of $C_{\mathrm{T}}(\mathrm{dust}) \simeq 0.4 \leq C_{\mathrm{T}}(\mathrm{gas+dust})$ in our simulation as shown in Figure 9. This result suggests the presence of dust-free gas, possibly located in the broad line region (BLR), is responsible for part of the X-ray absorption (see also Schnorr-Müller et al. 2016). Observationally, using X-ray observations, Markowitz et al. (2014) found evidence of occultation events in the X-rays, and the locations of those gas clumps are in the dust-free region or the inner edge of the dusty torus (e.g., Maiolino et al. 2010; Risaliti et al. 2007, 2011). In addition, Minezaki & Matsushita (2015) and Gandhi et al. (2015) have also suggested that the location of Fe Kα line emitting material could be between the BLR and the dusty torus. Several studies have also proposed that the AGN gas disk inside the dust sublimation radius could significantly contribute to the observed column density in Compton-thick AGN, since they are often found to have large inclination angles (e.g., Davies et al. 2015; Masini et al. 2016; Ramos Almeida & Ricci 2017).

We also check whether the similar trend of $C_{\mathrm{T}}(\mathrm{dust}) \leq C_{\mathrm{T}}(\mathrm{gas+dust})$ can be seen only using the MIR fluxes before the SED Decomposition. This is discussed in Appendix C.1.

Figure 8 also shows that both $C_{\mathrm{T}}(\mathrm{dust})$ and $C_{\mathrm{T}}(\mathrm{gas+dust})$ seem to have a suggestive peak at $\log L_{\mathrm{bol}} \simeq 43$, and they both seem decrease at lower luminosities. However, since the number of sample is limited in this bin range, we cannot confirm the statistical significance of this trend (see also the discussion in Appendix C.2).

4.4.3. *Comparison of* $C_{\mathrm{T}}(\mathrm{dust})$ *between unobscured and obscured AGN*

We compare here $C_{\mathrm{T}}(\mathrm{dust})$ for the different subgroups of AGN. The left panel of Figure 10 shows that the $C_{\mathrm{T}}(\mathrm{dust})$ of unobscured (blue) and obscured (red) AGN as a function of $L_{\mathrm{bol}}^{(\mathrm{AGN})}$. Although the scatter is large, the binned $C_{\mathrm{T}}(\mathrm{dust})$ of obscured AGN is always systematically higher than those of unobscured AGN.

The right panel of Figure 10 shows the distribution of $C_{\mathrm{T}}(\mathrm{dust})$ for unobscured (blue) and obscured (red) AGN. The $C_{\mathrm{T}}(\mathrm{dust})$ distribution for unobscured AGN is clustered at smaller values of $\langle C_{\mathrm{T}}(\mathrm{dust})\rangle = 0.41$, while the obscured AGN have a wider distribution of $C_{\mathrm{T}}(\mathrm{dust})$ reaching $C_{\mathrm{T}}(\mathrm{dust}) \simeq 1.0$. We apply the KS test for these two sample, and the null hypothesis p–value is 5.7×10^{-8}, and the KS-statistics is 0.24, suggesting that two distribution are significantly different.

One possible origin of the difference is that the smaller $C_{\mathrm{T}}(\mathrm{dust})$ for unobscured AGN could be due to larger $L_{\mathrm{bol}}^{(\mathrm{AGN})}$. However, as discussed in Section 4.4.1, the luminosity dependence of $C_{\mathrm{T}}(\mathrm{dust})$ is unlikely, and the KS test shows that the distribution of $C_{\mathrm{T}}(\mathrm{dust})$ for unobscured and obscured AGN is statistically significant even in each $L_{\mathrm{bol}}^{(\mathrm{AGN})}$ bin between $42.5 < \log(L_{\mathrm{bol}}^{(\mathrm{AGN})}/\mathrm{erg\ s^{-1}}) < 47$ with the p–value is $p < 10^{-5}$ between $42.5 < \log(L_{\mathrm{bol}}^{(\mathrm{AGN})}/\mathrm{erg\ s^{-1}}) < 45.5$ and $p = 0.02$ between $45.5 < \log(L_{\mathrm{bol}}^{(\mathrm{AGN})}/\mathrm{erg\ s^{-1}}) < 47$.

Another possible interpretation of the difference is a consequence of the selection of unobscured and obscured AGN. Several authors argue that AGN classification depends on the distribution of the $C_{\mathrm{T}}(\mathrm{dust})$; unobscured AGN would be preferentially observed from lower-$C_{\mathrm{T}}(\mathrm{dust})$ AGN, while obscured AGN from higher-$C_{\mathrm{T}}(\mathrm{dust})$ AGN (e.g., Ramos Almeida et al. 2011; Elitzur 2012; Ichikawa et al. 2015).

5. CONCLUSIONS

We have constructed the IR (3–500 μm) SED for 587 nearby AGN detected in the 70 month *Swift*/BAT all-sky survey. Using this almost complete (587 out of 606; 94%) sample, we have decomposed the IR (3–500 μm) SEDs into SB and AGN components. The decomposition enabled us to estimate the AGN contribution to the 12 μm ($L_{12\ \mu\mathrm{m}}^{(\mathrm{AGN})}$), MIR ($L_{\mathrm{MIR}}^{(\mathrm{AGN})}$), and the total IR luminosity ($L_{\mathrm{IR}}^{(\mathrm{AGN})}$), as well as the AGN luminosity contri-

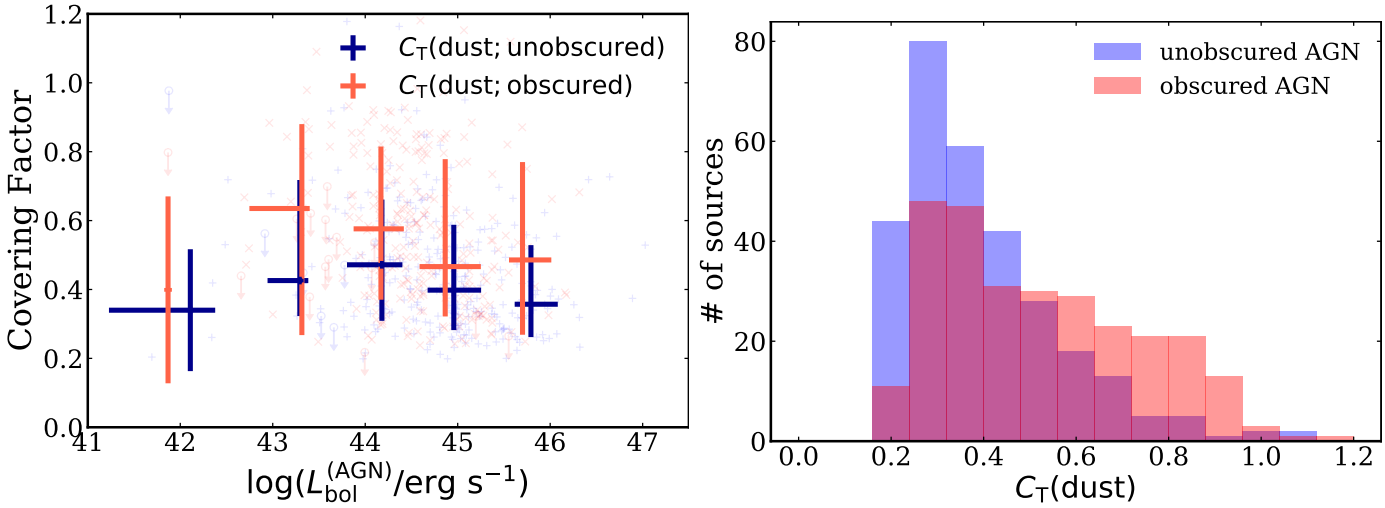

Figure 10. (Left) The dust covering factor ($C_{\rm T}$(dust)) of unobscured (blue) and obscured (red) AGN as a function of the bolometric luminosity. (Right) The distribution of $C_{\rm T}$(dust) of unobscured and obscured AGN.

bution to the 12 μm ($f_{\rm AGN}^{(12\mu{\rm m})}$), MIR ($f_{\rm AGN}^{(\rm MIR)}$), and the total IR emission ($f_{\rm AGN}^{(\rm IR)}$). Our results are summarized as follows:

1. The luminosity contribution of the AGN to the 12 μm, MIR, and total IR band flux increases with the 14–150 keV luminosity. For the most luminous sources, the AGN contribution is $\simeq$ 80% at the 12 μm, MIR, and $\simeq$ 50% at the total IR.

2. We find nine pure IR-AGN whose IR emission is dominated by the AGN torus at least up to 90 μm. These pure IR-AGN could be a good candidates to create templates of the IR AGN SED, up to 90 μm. Those sources could be easily selected using the color selection of $f_{70\ \mu{\rm m}}/f_{160\ \mu{\rm m}} > 1.0$ and $f_{22\ \mu{\rm m}}/f_{70\ \mu{\rm m}} > 1.0$.

3. We find a good luminosity correlation between the MIR and ultra hard X-ray band over 5 orders of magnitude [$41 < \log(L_{14-150}/\mathrm{erg\ s^{-1}}) < 46$]. Our slope is almost consistent with that obtained by studies carried out using high spatial resolution observations of nearby Seyfert galaxies, supporting our SED decomposition method, which would nicely estimate the intrinsic MIR emission without the contamination of star-formation from the host galaxies.

4. We find that the average of the covering factor of gas and dust inferred from X-ray observations always exceeds the one of dust torus covering factor, suggesting that the dust-free gas contributes to the absorption in the X-ray. This gas could be associated inside the dust sublimation radius, in agreement with previous observations based on X-ray occultation and spectral fitting studies of nearby AGN.

5. The luminosity-dependent trend of $C_{\rm T}$(dust) might be originated from the large scatter of the luminosity correlations between $L_{\rm IR}^{(\rm AGN;1-1000\mu m)}$ and L_{14-150}, and the trend would be disappeared once the scatter is removed.

6. The obscured AGN tend to have larger $C_{\rm T}$(dust) than unobscured AGN. This difference originates from the AGN classification, which depends on the distribution of the obscuring material.

We thank James Mullaney and Agnese Del Moro for providing the SB SED templates in this study, and Satoshi Takeshige for the technical discussion of IDL routine. We also thank Masatoshi Imanishi, Ryo Tazaki, and Daniel Asmus for fruitful discussions. KI thanks the Department of Astronomy at Kyoto university, where a part of the research was conducted. This study benefited from financial support from the Grant-in-Aid for JSPS fellow for young researchers (PD; KI), JSPS KAKENHI (18K13584; KI), and JST grant "Building of Consortia for the Development of Human Resources in Science and Technology" (KI). CR acknowledges the CONICYT+PAI Convocatoria Nacional subvencion a instalacion en la academia convocatoria año 2017 PAI77170080. FEB acknowledges support from CONICYT-Chile (Basal-CATA PFB-06/2007, FONDECYT Regular 1141218), the Ministry of Economy, Development, and Tourism's Millennium Science Initiative

through grant IC120009, awarded to The Millennium Institute of Astrophysics, MAS. K.O. is an International Research Fellow of the Japan Society for the Promotion of Science (JSPS) (ID: P17321).

REFERENCES

Alexander, D. M., & Hickox, R. C. 2012, NewAR, 56, 93

Alonso-Herrero, A., Ramos Almeida, C., Mason, R., et al. 2011, ApJ, 736, 82

Alonso-Herrero, A., Pereira-Santaella, M., Rieke, G. H., & Rigopoulou, D. 2012, ApJ, 744, 2

Alonso-Herrero, A., Esquej, P., Roche, P. F., et al. 2016, MNRAS, 455, 563

Asmus, D., Gandhi, P., Smette, A., Hönig, S. F., & Duschl, W. J. 2011, A&A, 536, A36

Asmus, D., Hönig, S. F., Gandhi, P., Smette, A., & Duschl, W. J. 2014, MNRAS, 439, 1648

Asmus, D., Gandhi, P., Hönig, S. F., Smette, A., & Duschl, W. J. 2015, MNRAS, 454, 766

Asmus, D., Hönig, S. F., & Gandhi, P. 2016, ApJ, 822, 109

Baumgartner, W. H., Tueller, J., Markwardt, C. B., et al. 2013, ApJS, 207, 19

Beckmann, V., Soldi, S., Ricci, C., et al. 2009, A&A, 505, 417

Beichman, C. A., Neugebauer, G., Habing, H. J., Clegg, P. E., & Chester, T. J. 1988, Infrared astronomical satellite (IRAS) catalogs and atlases. Volume 1: Explanatory supplement, 1

Brandl, B. R., Bernard-Salas, J., Spoon, H. W. W., et al. 2006, ApJ, 653, 1129

Burtscher, L., Meisenheimer, K., Tristram, K. R. W., et al. 2013, A&A, 558, A149

Burtscher, L., Hönig, S., Jaffe, W., et al. 2016, Proc. SPIE, 9907, 99070R

Casey, C. M. 2012, MNRAS, 425, 3094

Chary, R., & Elbaz, D. 2001, ApJ, 556, 562

Comastri, A., Gilli, R., Marconi, A., Risaliti, G., & Salvati, M. 2015, A&A, 574, L10

Cutri, R. M., Wright, E. L., Conrow, T., et al. 2013, Explanatory Supplement to the AllWISE Data Release Products, by R. M. Cutri et al. , 1

da Cunha, E., Charlot, S., & Elbaz, D. 2008, MNRAS, 388, 1595

Dale, D. A., Helou, G., Contursi, A., Silbermann, N. A., & Kolhatkar, S. 2001, ApJ, 549, 215

Davies, R. I., Burtscher, L., Rosario, D., et al. 2015, ApJ, 806, 127

Del Moro, A., Alexander, D. M., Mullaney, J. R., et al. 2013, A&A, 549, A59

Delvecchio, I., Gruppioni, C., Pozzi, F., et al. 2014, MNRAS, 439, 2736

Draine, B. T. 2003, ARA&A, 41, 241

Elitzur, M. 2012, ApJL, 747, L33

Feigelson, E. D., & Nelson, P. I. 1985, ApJ, 293, 192

Fuller, L., Lopez-Rodriguez, E., Packham, C., et al. 2016, MNRAS, 462, 2618

Gandhi, P., Horst, H., Smette, A., et al. 2009, A&A, 502, 457

Gandhi, P., Hönig, S. F., & Kishimoto, M. 2015, ApJ, 812, 113

García-Burillo, S., Combes, F., Ramos Almeida, C., et al. 2016, ApJL, 823, L12

García-González, J., Alonso-Herrero, A., Hernán-Caballero, A., et al. 2016, MNRAS, 458, 4512

González-Martín, O., Rodríguez-Espinosa, J. M., Díaz-Santos, T., et al. 2013, A&A, 553, A35

Griffin, M. J., Abergel, A., Abreu, A., et al. 2010, A&A, 518, L3

Hatziminaoglou, E., Fritz, J., Franceschini, A., et al. 2008, MNRAS, 386, 1252

Hernán-Caballero, A., Alonso-Herrero, A., Hatziminaoglou, E., et al. 2015, ApJ, 803, 109

Hönig, S. F., Kishimoto, M., Gandhi, P., et al. 2010, A&A, 515, A23

Hönig, S. F., Kishimoto, M., Antonucci, R., et al. 2012, ApJ, 755, 149

Hönig, S. F., Kishimoto, M., Tristram, K. R. W., et al. 2013, ApJ, 771, 87

Hönig, S. F., Gandhi, P., Asmus, D., et al. 2014, MNRAS, 438, 647

Ichikawa, K., Ueda, Y., Terashima, Y., et al. 2012, ApJ, 754, 45

Ichikawa, K., Imanishi, M., Ueda, Y., et al. 2014, ApJ, 794, 139

Ichikawa, K., Packham, C., Ramos Almeida, C., et al. 2015, ApJ, 803, 57

Ichikawa, K., Ricci, C., Ueda, Y., et al. 2017, ApJ, 835, 74

Ichikawa, K., & Inayoshi, K. 2017, ApJL, 840, L9

Imanishi, M., Nakanishi, K., Izumi, T., & Wada, K. 2018, ApJL, 853, L25

Inayoshi, K., & Haiman, Z. 2016, ApJ, 828, 110

Isobe, T., Feigelson, E. D., & Nelson, P. I. 1986, ApJ, 306, 490

Isobe, T., Feigelson, E. D., Akritas, M. G., & Babu, G. J. 1990, ApJ, 364, 104

Jaffe, W., Meisenheimer, K., Röttgering, H. J. A., et al. 2004, Nature, 429, 47
Jun, H. D., Im, M., Lee, H. M., et al. 2015, ApJ, 806, 109
Kirkpatrick, A., Pope, A., Sajina, A., et al. 2015, ApJ, 814, 9
Kormendy, J., & Ho, L. C. 2013, ARA&A, 51, 511
Koss, M. J., Assef, R., Baloković, M., et al. 2016, ApJ, 825, 85
Koss, M., Trakhtenbrot, B., Ricci, C., et al. 2017, ApJ, 850, 74
Krolik, J. H., & Begelman, M. C. 1986, ApJL, 308, L55
Lamperti, I., Koss, M., Trakhtenbrot, B., et al. 2017, MNRAS, 467, 540
Lani, C., Netzer, H., & Lutz, D. 2017, MNRAS, 471, 59
Lavalley, M., Isobe, T., & Feigelson, E. 1992, Astronomical Data Analysis Software and Systems I, 25, 245
López-Gonzaga, N., Burtscher, L., Tristram, K. R. W., Meisenheimer, K., & Schartmann, M. 2016, A&A, 591, A47
Lopez-Rodriguez, E., Alonso-Herrero, A., Diaz-Santos, T., et al. 2018, MNRAS, 478, 2350
Lusso, E., Hennawi, J. F., Comastri, A., et al. 2013, ApJ, 777, 86
Lutz, D., Maiolino, R., Spoon, H. W. W., & Moorwood, A. F. M. 2004, A&A, 418, 46
Lyu, J., Rieke, G. H., & Alberts, S. 2016, ApJ, 816, 85
Lyu, J., Rieke, G. H., & Shi, Y. 2017, ApJ, 835, 257
Maiolino, R., Shemmer, O., Imanishi, M., et al. 2007, A&A, 468, 979
Maiolino, R., Risaliti, G., Salvati, M., et al. 2010, A&A, 517, A47
Marconi, A., Risaliti, G., Gilli, R., et al. 2004, MNRAS, 351, 169
Markowitz, A. G., Krumpe, M., & Nikutta, R. 2014, MNRAS, 439, 1403
Martínez-Paredes, M., Aretxaga, I., Alonso-Herrero, A., et al. 2017, MNRAS, 468, 2
Masini, A., Comastri, A., Baloković, M., et al. 2016, A&A, 589, A59
Mateos, S., Carrera, F. J., Alonso-Herrero, A., et al. 2016, ApJ, 819, 166
Matsuoka, K., & Woo, J.-H. 2015, ApJ, 807, 28
McLure, R. J., & Dunlop, J. S. 2004, MNRAS, 352, 1390
Meléndez, M., Mushotzky, R. F., Shimizu, T. T., Barger, A. J., & Cowie, L. L. 2014, ApJ, 794, 152
Mineo, S., Gilfanov, M., & Sunyaev, R. 2012, MNRAS, 419, 2095
Minezaki, T., & Matsushita, K. 2015, ApJ, 802, 98
Mullaney, J. R., Alexander, D. M., Goulding, A. D., & Hickox, R. C. 2011, MNRAS, 414, 1082
Murakami, H., Baba, H., Barthel, P., et al. 2007, PASJ, 59, S369
Murphy, E. J., Chary, R.-R., Dickinson, M., et al. 2011, ApJ, 732, 126
Mushotzky, R. F., Shimizu, T. T., Meléndez, M., & Koss, M. 2014, ApJL, 781, L34
Nenkova, M., Sirocky, M. M., Ivezić, Ž., & Elitzur, M. 2008, ApJ, 685, 147
Nenkova, M., Sirocky, M. M., Nikutta, R., Ivezić, Ž., & Elitzur, M. 2008, ApJ, 685, 160
Netzer, H. 1987, MNRAS, 225, 55
Netzer, H. 2003, ApJL, 583, L5
Netzer, H., Lutz, D., Schweitzer, M., et al. 2007, ApJ, 666, 806
Netzer, H. 2015, ARA&A, 53, 365
Netzer, H., Lani, C., Nordon, R., et al. 2016, ApJ, 819, 123
Novak, G. S. 2013, arXiv:1310.3833
Oh, K., Koss, M., Markwardt, C. B., et al. 2018, arXiv:1801.01882
Packham, C., Radomski, J. T., Roche, P. F., et al. 2005, ApJL, 618, L17
Poglitsch, A., Waelkens, C., Geis, N., et al. 2010, A&A, 518, L2
Raban, D., Jaffe, W., Röttgering, H., Meisenheimer, K., & Tristram, K. R. W. 2009, MNRAS, 394, 1325
Radomski, J. T., Packham, C., Levenson, N. A., et al. 2008, ApJ, 681, 141-150
Ramos Almeida, C., Levenson, N. A., Alonso-Herrero, A., et al. 2011, ApJ, 731, 92
Ramos Almeida, C., & Ricci, C. 2017, Nature Astronomy, 1, 679
Ricci, C., Paltani, S., Awaki, H., et al. 2013, A&A, 553, A29
Ricci, C., Ueda, Y., Koss, M. J., et al. 2015, ApJL, 815, L13
Ricci, C., Trakhtenbrot, B., Koss, M. J., et al. 2017b, ApJS, 233, 17
Ricci, C., Trakhtenbrot, B., Koss, M. J., et al. 2017a, Nature, 549, 488
Richards, G. T., Lacy, M., Storrie-Lombardi, L. J., et al. 2006, ApJS, 166, 470
Rieke, G. H., Ressler, M. E., Morrison, J. E., et al. 2015, PASP, 127, 665
Risaliti, G., Elvis, M., & Gilli, R. 2002, ApJL, 566, L67
Risaliti, G., Elvis, M., Fabbiano, G., et al. 2007, ApJL, 659, L111
Risaliti, G., Nardini, E., Salvati, M., et al. 2011, MNRAS, 410, 1027
Rosario, D. J., Santini, P., Lutz, D., et al. 2012, A&A, 545, A45
Rosario, D. J., Burtscher, L., Davies, R. I., et al. 2018, MNRAS, 473, 5658

Sajina, A., Yan, L., Armus, L., et al. 2007, ApJ, 664, 713
Schnorr-Müller, A., Davies, R. I., Korista, K. T., et al. 2016, MNRAS, 462, 3570
Shimizu, T. T., Meléndez, M., Mushotzky, R. F., et al. 2016, MNRAS, 456, 3335
Shimizu, T. T., Mushotzky, R. F., Meléndez, M., et al. 2017, MNRAS, 466, 3161
Simpson, C. 2005, MNRAS, 360, 565
Stalevski, M., Ricci, C., Ueda, Y., et al. 2016, MNRAS, 458, 2288
Stanley, F., Harrison, C. M., Alexander, D. M., et al. 2015, MNRAS, 453, 591
Symeonidis, M., Giblin, B. M., Page, M. J., et al. 2016, MNRAS, 459, 257
Trakhtenbrot, B. 2014, ApJL, 789, L9
Tran, Q. D., Lutz, D., Genzel, R., et al. 2001, ApJ, 552, 527
Treister, E., Krolik, J. H., & Dullemond, C. 2008, ApJ, 679, 140-148
Tristram, K. R. W., Burtscher, L., Jaffe, W., et al. 2014, A&A, 563, A82
Tueller, J., Mushotzky, R. F., Barthelmy, S., et al. 2008, ApJ, 681, 113-127
Ueda, Y., Akiyama, M., Ohta, K., & Miyaji, T. 2003, ApJ, 598, 886
Ueda, Y., Hiroi, K., Isobe, N., et al. 2011, PASJ, 63, S937
Ueda, Y., Akiyama, M., Hasinger, G., Miyaji, T., & Watson, M. G. 2014, ApJ, 786, 104
Wright, E. L., Eisenhardt, P. R. M., Mainzer, A. K., et al. 2010, AJ, 140, 1868
Xu, L., Rieke, G. H., Egami, E., et al. 2015, ApJS, 219, 18
Yu, Q., & Tremaine, S. 2002, MNRAS, 335, 965

Table 1. Column descriptions for the IR catalog of *Swift*/BAT 70 Month AGN survey

Col. #	Header Name	Format	Unit	Description
1	objID	string	–	*Swift*/BAT ID as shown in Baumgartner et al. (2013)
2	ctpt1	string	–	optical counterpart name
3	z	float	–	redshift
4	NH_log	float	–	logarithmic column density ($\log N_{\rm H}/{\rm cm}^{-2}$)
5	lbat_log	float	–	absorption corrected logarithmic 14–150 keV luminosity ($\log L_{14-150}/{\rm erg\ s}^{-1}$)
6	lbol_const_log	float	–	logarithmic bolometric AGN luminosity ($\log(L_{\rm bol}^{\rm (AGN)}/{\rm erg\ s}^{-1})$)
7	lbol_log	float	–	logarithmic bolometric AGN luminosity ($\log(L_{\rm bol}^{\rm (M04)}/{\rm erg\ s}^{-1})$) using Marconi et
8 (9)	fnu3p4_(err)_fqualmod	float	Jy	3.4 μm profile-fitting flux density (error) obtained from *WISE*
10 (11)	fnu4p6_(err)_fqualmod	float	Jy	4.6 μm profile-fitting flux density (error) obtained from *WISE*
12 (13)	fnu9a_(err)_fqualmod	float	Jy	9.0 μm flux density (error) obtained from *AKARI*/IRC
14 (15)	fnu12wipf_(err)_fqualmod	float	Jy	12 μm flux density (error)
16	fnu12wipcatalog	string	–	reference catalogs for 12 μm: W=*WISE*, Ip=*IRAS*/PSC, If=*IRAS*/FSC
17 (18)	fnu18a_(err)_fqualmod	float	Jy	18.0 μm flux density (error) obtained from *AKARI*
19 (20)	fnu22w_(err)_fqualmod	float	Jy	22 μm profile-fitting flux density (error) obtained from *WISE*
21 (22)	fnu25ipf_(err)_fqualmod	float	Jy	25 μm flux density (error)
23	fnu25ipfcatalog	string	–	reference catalogs for 25 μm: Ip=*IRAS*/PSC, If=*IRAS*/FSC
24 (25)	fnu60ipf_(err)_fqualmod	float	Jy	60 μm flux density (error)
26	fnu60ipfcatalog	string	–	reference catalogs for 60 μm: Ip=*IRAS*/PSC, If=*IRAS*/FSC
27 (28)	fnu65a_(err)_fqualmod	float	Jy	65 μm flux density (error) obtained from *AKARI*/FIS
29 (30)	fnu70p_(err)_fqualmod	float	Jy	70 μm flux density (error) obtained from *Herschel*/PACS
31 (32)	fnu90a_(err)_fqualmod	float	Jy	90 μm flux density (error) obtained from *AKARI*/FIS
33 (34)	fnu100ipf_(err)_fqualmod	float	Jy	100 μm flux density (error)
35	fnu100ipfcatalog	string	–	reference catalogs for 100 μm: Ip=*IRAS*/PSC, If=*IRAS*/FSC
36 (37)	fnu140a_(err)_fqualmod	float	Jy	140 μm flux density (error) obtained from *AKARI*/FIS
38 (39)	fnu160pa_(err)_fqualmod	float	Jy	160 μm flux density (error)
40	fnu160pacatalog	string	–	reference catalogs for 160 μm: P=*Herschel*/PACS, A=*AKARI*/FIS
41 (42)	fnu250s_(err)_fqualmod	float	Jy	250 μm flux density (error) obtained from *Herschel*/SPIRE
43 (44)	fnu350s_(err)_fqualmod	float	Jy	350 μm flux density (error) obtained from *Herschel*/SPIRE
45 (46)	fnu500s_(err)_fqualmod	float	Jy	500 μm flux density (error) obtained from *Herschel*/SPIRE
47	l12_AGN_afSta15_log	float	–	Logarithmic decomposed 12 μm AGN luminosity $\log(L_{12\ \mu{\rm m}}^{\rm (AGN)}/{\rm erg\ s}^{-1})$
48	lMIR_AGN_afSta15_log	float	–	Logarithmic decomposed MIR AGN luminosity $\log(L_{\rm MIR}^{\rm (AGN)}/{\rm erg\ s}^{-1})$
49	lIR_AGN_afSta15_log	float	–	Logarithmic decomposed total IR luminosity $\log(L_{\rm IR}^{\rm (AGN)}/{\rm erg\ s}^{-1})$
50	l12AGNratio_afSta15	float	–	$f_{\rm AGN}^{(12\mu{\rm m})}$
51	AGNpercentage_MIR_afSta15	float	–	$f_{\rm AGN}^{\rm (MIR)}$
52	AGNpercentage_afSta15	float	–	$f_{\rm AGN}^{\rm (IR)}$
53	flag_upperlimit	int	–	Flag of AGN: detection (= 0), upper-limit (= 1), and lower-limit (= −1)
54	R_Sta16_afSta15_log	float	–	$\log R = \log(L_{\rm IR}^{\rm (AGN)}/L_{\rm bol}^{\rm (AGN)})$
55	CF_Sta16_tau9p7eq3_afSta15	float	–	$C_{\rm T}$(dust)
56	SBtemplate_afSta15	string	–	SB template used for the SED fitting this study: SB1–SB5

Notes. The detail of the selection of the flux is compiled in Section 2. The full catalog is available as a machine readable electronic table.

Table 2. Equations of the correlation in this study

(1)	(2)	(3)	(4)	(5)
Y	X	a	b	Reference
$\log\left(\frac{L_{12\ \mu\mathrm{m}}^{(\mathrm{AGN})}}{10^{43}\ \mathrm{erg/s}}\right)$	$\log\left(\frac{L_{14-150}}{10^{43}\ \mathrm{erg/s}}\right)$	-0.24 ± 0.03	1.08 ± 0.03	Section 4.3
$\log\left(\frac{L_{\mathrm{MIR}}^{(\mathrm{AGN})}}{10^{43}\ \mathrm{erg/s}}\right)$	$\log\left(\frac{L_{14-150}}{10^{43}\ \mathrm{erg/s}}\right)$	-0.05 ± 0.03	1.06 ± 0.03	Section 4.3
$\log R$	$\log\left(\frac{L_{\mathrm{bol}}^{(\mathrm{AGN})}}{\mathrm{erg\ s^{-1}}}\right)$	4.52 ± 1.25	-0.12 ± 0.03	Section 4.4

Notes.— Correlation properties between two physical values. Columns: (1) Y variable; (2) X variable; (3) regression intercept (a) and its 1σ uncertainty; (4) slope (b) and its 1σ uncertainty. Equation is represented as $Y = a + bX$; (5) Reference of the details on each Equation.

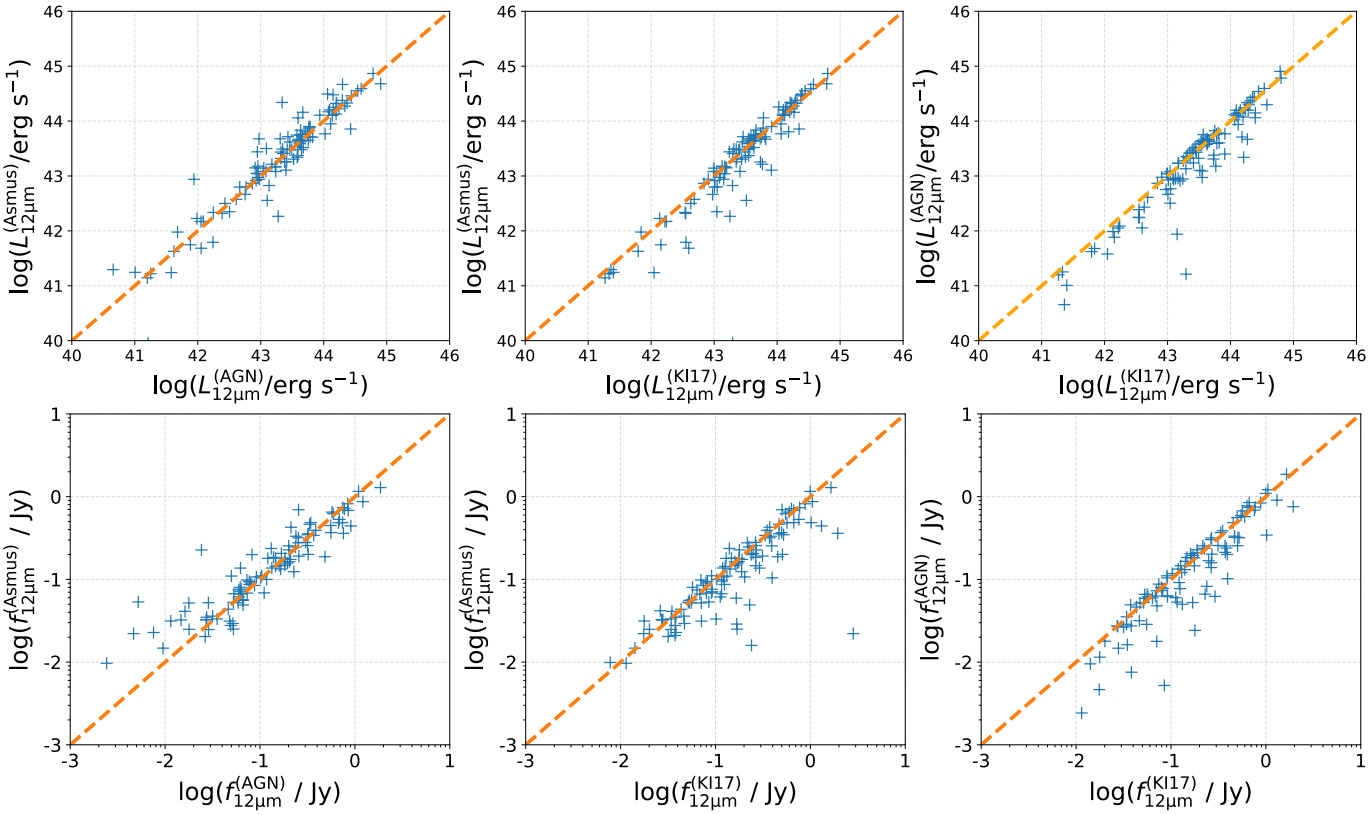

Figure 11. (Top) Scatter plot of the 12 μm luminosities obtained from high spatial resolution MIR observations ($L_{12\mu\mathrm{m}}^{(\mathrm{Asmus})}$; Asmus et al. 2014, 2015), this study after the SED decomposition ($L_{12\ \mu\mathrm{m}}^{(\mathrm{AGN})}$), and before the SED decomposition ($L_{12\mu\mathrm{m}}^{(\mathrm{KI17})}$; Ichikawa et al. 2017). The blue cross represents the individual sources, and the orange dashed line represents the 1:1 relation. Each panel shows the luminosity relation between $L_{12\mu\mathrm{m}}^{(\mathrm{Asmus})}$ and $L_{12\ \mu\mathrm{m}}^{(\mathrm{AGN})}$ (Left), $L_{12\mu\mathrm{m}}^{(\mathrm{Asmus})}$ and $L_{12\mu\mathrm{m}}^{(\mathrm{KI17})}$ (Middle), $L_{12\ \mu\mathrm{m}}^{(\mathrm{AGN})}$ and $L_{12\mu\mathrm{m}}^{(\mathrm{KI17})}$ (Right). (Bottom) Same plots as top but for 12 μm flux densities.

APPENDIX

A. COMPARISON WITH THE STUDIES FROM THE LITERATURE

A.1. *Comparison with the high spatial resolution flux obtained with ground-based 8m class telescopes*

Here we compare the results in this study with the high spatial resolution observations by Asmus et al. (2014, 2015). Out of 122 high spatial resolution sources, we found 112 sources also used in this study. The remaining 10 sources were not found because they are located in the low galactic latitude of $|b| < 10^{\circ}$, where we initially removed from the parent sample as discussed in Ichikawa et al. (2017).

The top left panel of Figure 11 shows the 12 μm luminosity correlation between the high spatial resolution MIR observations ($L_{12\mu\mathrm{m}}^{(\mathrm{Asmus})}$; Asmus et al. 2014, 2015) and this study after the SED decomposition ($L_{12\ \mu\mathrm{m}}^{(\mathrm{AGN})}$). The figure clearly shows that our decomposition method successfully follows the one-by-one relation with the high spatial resolution observations down to $\log(L_{12\ \mu\mathrm{m}}^{(\mathrm{AGN})}/\mathrm{erg\ s^{-1}}) \simeq 41.0$. The average of two parameters of $\left\langle \log L_{12\mu\mathrm{m}}^{(\mathrm{Asmus})}/L_{12\ \mu\mathrm{m}}^{(\mathrm{AGN})} \right\rangle = 0.05$. The standard deviation is $\sigma = 0.36$.

The top middle and right panels of Figure 11 shows the luminosity relation between $L_{12\mu\mathrm{m}}^{(\mathrm{Asmus})}$, $L_{12\ \mu\mathrm{m}}^{(\mathrm{AGN})}$, and the low-resolution 12 μm luminosity before the SED decomposition ($L_{12\mu\mathrm{m}}^{(\mathrm{KI17})}$), which is taken from Ichikawa et al. (2017). Both panels show that the points are distributed equal or below the one-by-one relations and suggestive of the contamination of the host galaxy component in $L_{12\mu\mathrm{m}}^{(\mathrm{KI17})}$. The mean and standard devition is $\left\langle \log L_{12\mu\mathrm{m}}^{(\mathrm{Asmus})}/L_{12\mu\mathrm{m}}^{(\mathrm{KI17})} \right\rangle = -0.10 \pm 0.43$. This shows that the correlation between $L_{12\mu\mathrm{m}}^{(\mathrm{Asmus})}$ and $L_{12\ \mu\mathrm{m}}^{(\mathrm{AGN})}$ is tighter than that of $L_{12\mu\mathrm{m}}^{(\mathrm{Asmus})}$ and $L_{12\mu\mathrm{m}}^{(\mathrm{KI17})}$, indicating that our decomposition method nicely reduces the contamination in the 12 μm band from the host galaxies.

The bottom panels of Figure 11 show the same relation as those in the top panels, but for 12 μm flux densities. All three panels also show the similar trend as the luminosity relations. One notable difference is that the flux density of the high spatial resolution observation ($f_{12\mu\mathrm{m}}^{(\mathrm{Asmus})}$) shows a decline of the number of sources at around $f_{12\mu\mathrm{m}}^{(\mathrm{Asmus})} \simeq 10^{-2}$ Jy. This is almost consistent with the lower-bound of the flux density observable with ground-based 8m class telescopes with significant signal-to-noise ratio (Asmus et al. 2014). Our study can explore flux densities down to 10^{-3} Jy, which is equivalent to the detection limit of the *WISE* W3 (12 μm) band. This is one of the advantages of the SED decomposition method using low-resolution, but sensitive space IR satellites compared to the ground based studies.

A.2. *Comparison with different models from the literature*

In this appendix we briefly compare the IR AGN luminosity obtained in this study and the ones obtained in Shimizu et al. (2017). They applied a different IR SED model to the IR dataset, which is similar with ours, obtained from the *Herschel* observations in the *Swift*/BAT 58-month AGN catalog to study mainly the global star-forming properties in the host galaxies. Instead of using the AGN/host galaxy templates, they provided a function of hot dust and the host galaxy respectively by following Casey (2012) and their functions are given by

$$f(\nu) = N_{\mathrm{pl}} \left(\frac{\nu}{\nu_{\mathrm{c}}}\right) e^{-(\nu_{\mathrm{c}}/\nu)^2} + S_{\mathrm{MBB}}(\nu, M_{\mathrm{dust}}, T_{\mathrm{dust}}), \tag{A1}$$

where the first section stands for the AGN component with the normalization N_{pl}, cut-off frequency ν_{c}, and the second section represents the host galaxy component of a single modified black body with the parameter of dust mass M_{dust} and the dust temperature T_{dust}. The fitting method used in their study is also different with ours. They use a Bayesian framework with a Markov chain Monte Carlo to obtain the posterior probability distribution function, and then use the median to obtain the best fitted parameters. Out of 307 sources in their sample, 204 sources have at least one *Herschel* detections and the reliable fitting quality (`lir_agn_flag`= 0). After the cross-matching with our sample, we found 180 sources in common. Again, the removed 24 sources are located in the low galactic latitude of $|b| < 10^{\circ}$.

Since Shimizu et al. (2017) do not provide any 12 μm AGN flux or luminosity, we compare the total IR AGN luminosity obtained from their AGN component. The left panel of Figure 12 shows the correlation between the IR AGN luminosities obtained from Shimizu et al. (2017) ($L_{\mathrm{IR}}^{(\mathrm{AGN;Shimizu})}$) and the ones from this study. We find a good luminosity correlation between $L_{\mathrm{IR}}^{(\mathrm{AGN;Shimizu})}$ and $L_{\mathrm{IR}}^{(\mathrm{AGN})}$. The Spearman's ran coefficient is 0.91, and null hypothesis probability is $P = 4.9 \times 10^{-69}$, suggesting the correlation is significant. The average of the distribution of $r = \log(L_{\mathrm{IR}}^{(\mathrm{AGN;Shimizu})}/L_{\mathrm{IR}}^{(\mathrm{AGN})})$ is also shown in the right panel of Figure 12. We do not find any systematic offset between the two methods ($\mu = 0.05$) with a standard deviation of $\sigma = 0.22$ dex. Since there are several outliers

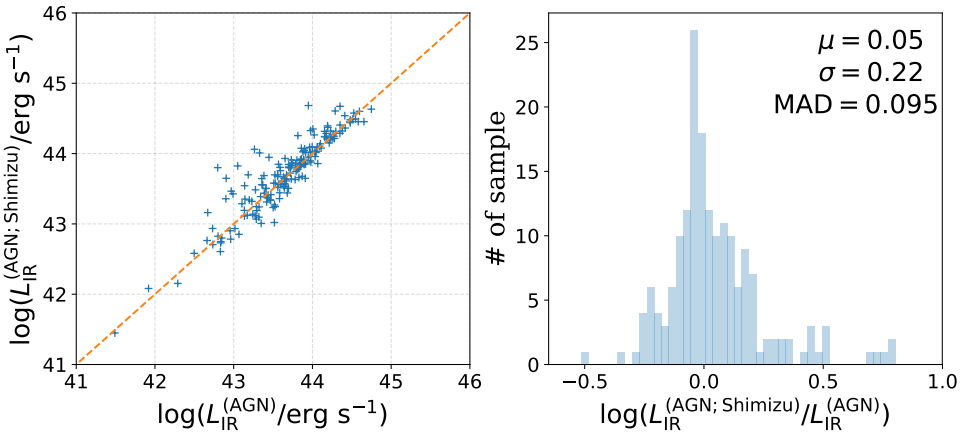

Figure 12. (Left) Scatter plot of total IR AGN luminosities obtained from Shimizu et al. (2017) ($L_{\rm IR}^{\rm (AGN;Shimizu)}$) and ones obtained from this study ($L_{\rm IR}^{\rm (AGN)}$). The blue cross represents the individual sources, and the orange dashed line represents the 1:1 relation. (Right) Histogram of $r = \log(L_{\rm IR}^{\rm (AGN;Shimizu)}/L_{\rm IR}^{\rm (AGN)})$. The mean μ, standard deviation σ, and median absolute deviation (MAD) of r are also shown in the panel.

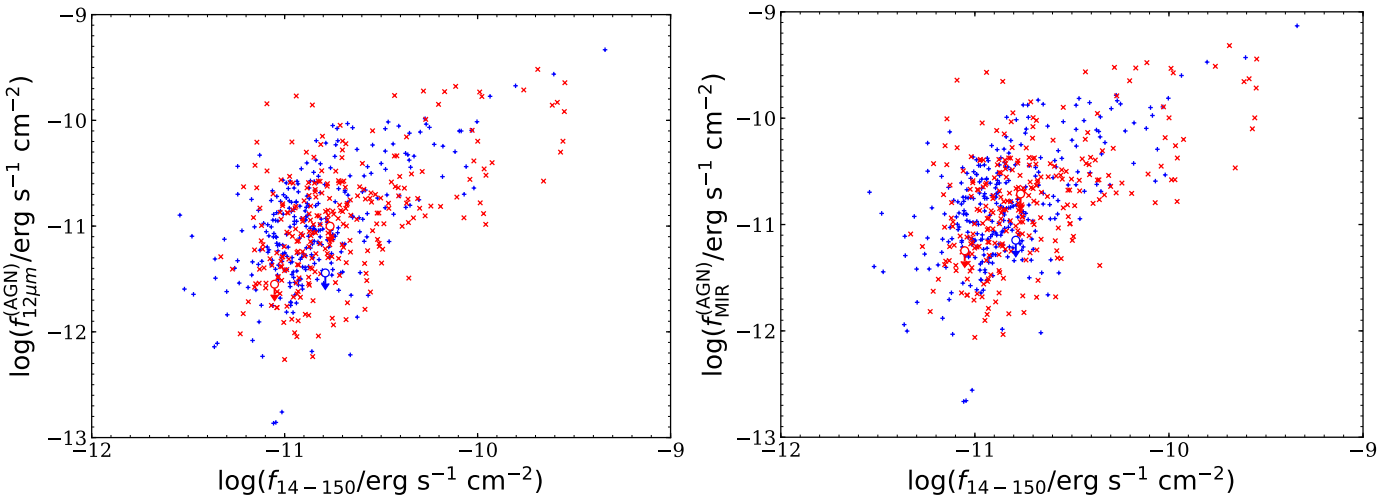

Figure 13. Correlation between the fluxes at 12 μm, MIR band and 14–150 keV. Blue and red cross represents unobscured and obscured AGN, respectively.

with $\log(L_{\rm IR}^{\rm (AGN;Shimizu)}/L_{\rm IR}^{\rm (AGN)}) > 0.3$, we also compute the median absolute deviation (MAD) and the value is MAD= 0.095 dex, which is smaller by a factor of two than the standard deviation. As already mentioned in Shimizu et al. (2017), their model allows the power-law component to extend to longer wavelengths, which would return slightly larger AGN luminosities with $\log(L_{\rm IR}^{\rm (AGN;Shimizu)}/L_{\rm IR}^{\rm (AGN)}) > 0.3$ for some cases. Those sources are actually seen in Figure 12 but only for a few percentages of the sample. Thus, we conclude that, although the different fitting methods and the template, each model returns the consensus results for the estimation of the IR AGN luminosities.

B. FLUX CORRELATION BETWEEN 12 μM, MIR, AND 14–150 KEV BANDS

Figure 13 shows the flux correlation between the AGN 12 μm, MIR, and 14–150 keV bands, showing a clear correlation between the two bands even in the flux-flux plane. The Spearman's ran coefficient is 0.43 and the null hypothetical probability is $P = 10^{-28}$ for both flux-flux correlations, suggesting the correlation is significant. The slope of $b = 1.48$ for the AGN 12 μm band and $b = 1.49$ for the AGN MIR band, respectively. As we discussed in Ichikawa et al. (2017), there is a clear decline of the number of sources at $f_{14-150} < 10^{-11}$ erg s^{-1} cm^{-2}, while MIR flux can go down to

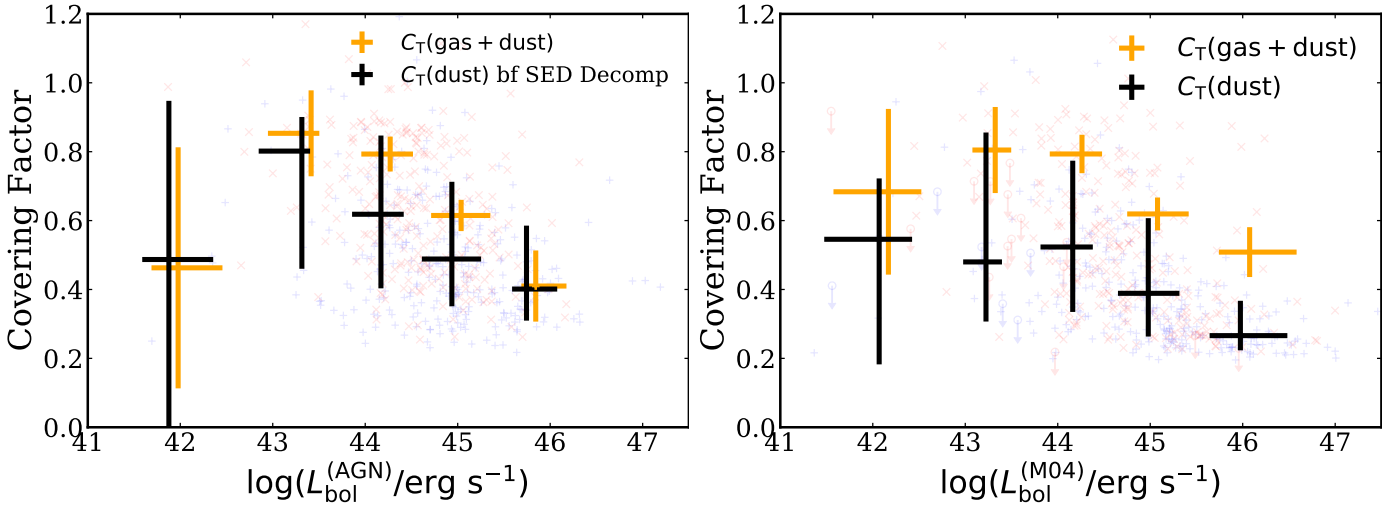

Figure 14. Same as Figure 8, but using the different estimation for the values. (Left) the covering factors used here are based on the estimation using the observed 12 μm luminosities in Ichikawa et al. (2017) before the IR SED decomposition. (Right) the bolometric corrections used are dependent on the bolometric luminosity ($L_{bol}^{(M04)}$; Marconi et al. 2004), not the constant bolometric correction.

3×10^{-13} erg s^{-1} cm^{-2}, which is the typical MIR band detection limit. This trend suggests that the sample is limited by the X-ray flux detection limit.

C. COMPARISON OF C_T AND $L_{bol}^{(AGN)}$ RELATION USING DIFFERENT VALUES

C.1. C_T(dust) *Estimated from the Observed 12 μm Luminosity*

It is important to check whether the same result in Figure 8 is obtained using the MIR fluxes without host galaxy subtraction. To achieve this, we estimate the total IR AGN luminosity by assuming that the observed 12 μm luminosity originates from the AGN emission. Then we use the conversion factor of $L_{IR}^{(AGN;1-1000\mu m)}/L_{12\ \mu m}^{(AGN)} = 2.77$ estimated from the AGN template in this study. The calculation of the R, and then C_T(dust) is performed in the same manner as we discussed in Section 4.4. The left panel of Figure 14 shows the relation of C_T and $L_{bol}^{(AGN)}$ using the C_T(dust) estimated above. It clearly shows that while the result of C_T(dust) $< C_T$(gas + dust) holds between $43.5 < \log L_{bol}^{(AGN)} < 45.5$, C_T(dust) becomes almost equal to C_T(gas + dust) at the luminosity bin of $42.5 < \log L_{bol}^{(AGN)} < 43.5$, which is not seen in Figure 8. We also apply the KS-test between C_T(dust) and C_T(gas + dust) for each $L_{bol}^{(AGN)}$ luminosity bin. In order to apply the KS-test, we make a Gaussian distribution of C_T(gas + dust) in which the central value is the average of C_T(gas + dust) and the 1σ is the standard deviation of C_T(gas + dust), and the number of sources are same as C_T(dust) in the same $L_{bol}^{(AGN)}$ bin. As a result, we find a significant difference for the luminosity bins between $43.5 < \log L_{bol}^{(AGN)} < 45.5$ with p-values of $p < 10^{-30}$, while the clear significance is not obtained at the luminosity bin of $\log L_{bol}^{(AGN)} < 43.5$ ($p > 0.5$) and $45.5 < \log L_{bol}^{(AGN)}$ ($p = 0.26$). This difference would originate from the flux subtraction after the SED decomposition especially at the lower AGN luminosity end, suggesting their importance and effect to estimate the dust covering factor.

C.2. *Dependence of the Bolometric Corrections*

Here we summarize whether different bolometric correction can affect the relation shown in Figure 8. In this study, following the method used in Ricci et al. (2017a), we use the constant bolometric correction of $L_{bol}^{(AGN)}/L_{14-150} = 8.47$, which is based on $L_{bol}^{(AGN)}/L_{2-10} = 20$ under the assumption of $\Gamma = 1.8$; the median value of the *Swift*/BAT 70-month AGN sample (Ricci et al. 2017b). On the other hand, Marconi et al. (2004) account for variations in AGN SEDs to obtain the bolometric correction with AGN luminosity. They assume a varying relation between optical/UR and X-ray luminosity, which is called a luminosity-dependent bolometric correction. This gives the larger bolometric correction than the constant one in higher AGN luminosity end, which would make average $L_{bol}^{(AGN)}$ larger, and C_T smaller.

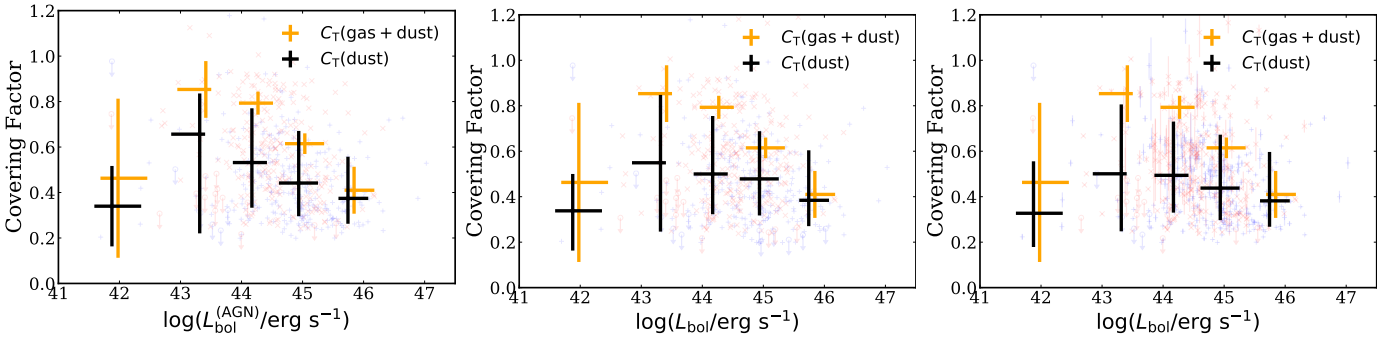

Figure 15. Same as Figure 8, but using the different set of free-parameters for (Left) addition of the dust extinction, and (Middle) fixed the power-law index $\alpha_1 = 1.8$. (Right) same as Figure 8, but using the averaged C_T(dust) of the SB templates as discussed in Appendix C.4.

The right panel of Figure 14 shows the same plot of Figure 8, but for the one using the luminosity-dependent bolometric correction of (Marconi et al. 2004). As expected from the luminosity-dependent bolometric correction, the distribution is slightly shifted into the right and bottom direction in the Figure. Actually, the median values of AGN bolometric luminosity and C_T(dust) changes from $(\log L_{bol}^{(AGN)}, C_T(\mathrm{dust})) = (44.65, 0.46)$ to $(\log L_{bol}^{(AGN;M04)}, C_T(\mathrm{dust})) = (44.79, 0.39)$.

The figure clearly holds the trend of $C_T(\mathrm{gas+dust}) \geq C_T(\mathrm{dust})$ over the entire AGN luminosity range. On the other hand, the slight decline of the C_T(dust) at the lowest AGN bolometric luminosity bin disappears in Figure 14. This is mainly because of the small statistics in the lowest luminosity bin and some sources are shifted into the higher luminosity bin because of the larger bolometric correction by Marconi et al. (2004).

C.3. *Dependence of Additional Torus Parameters*

We here discuss how the dust covering factor changes when we change the set of the torus parameters. In this study we have only considered the spectral power-law index (α_1) at $\lambda < 19$ μm for high luminosity end with $\log L_{14-150} > 44$, but not considered the dust extinction for obscured AGN, which could be one of the most significant parameters shaping the torus SEDs. The left panel of Figure 15 shows the C_T(dust) as a function of $L_{bol}^{(AGN)}$ after addition of the dust extinction for obscured AGN using the absorption profile of Draine (2003) (see also Mullaney et al. 2011). C_T(dust) becomes slightly larger, but the overall sense does not change. The middle panel shows the same plot using a fixed power-law index $\alpha_1 = 1.8$ for all sources without the dust extinction. The C_T(dust) shows a relatively flatter distribution compared to Figure 8, but the overall trend of $C_T(\mathrm{dust}) < C_T(\mathrm{gas+dust})$ still holds.

C.4. *Dependence of Other SB Templates*

In this study, we used the best SB template based on the lowest χ^2 value as discussed in Section 3. However, the other SB templates sometimes show similar quality fitting results with small $\Delta\chi^2$ between the best one and the other. Therefore, we here investigate how the result could be affected by using such different SB templates. We consider here that the fitting result is indistinguishable if the $\Delta\chi^2$ between the best fitting SB template and the other SB ones are smaller than the χ^2_{max}, which is the maximum allowed χ^2 corresponding the p-value= 0.05 of χ^2 distributions with the degree of freedom for each source. If each source has indistinguishable SB templates, we then measure the averaged C_T(dust) and the standard deviation ΔC_T(dust). The right panel of Figure 15 shows the result using the averaged C_T(dust) here, and the binned values of C_T(dust) becomes slightly smaller compared to the original ones.

D. FULL LIST OF SEDS

The full list of SEDs with the fitting results is available from the link here[5].

[5] http://www.kusastro.kyoto-u.ac.jp/~ichikawa/ms_KI_20180307_fullSED.pdf